Earthq Eng & Eng Vib (2017) 16: 311-328 **DOI**:10.1007/s11803-017-0384-y

Green's function of multi-layered poroelastic half-space for models of ground vibration due to railway traffic

Wang Futong[1,2†], Tao Xiaxin[1,3‡], Xie Lili[1,3‡] and Siddharthan Raj[4‡]

1. *Institute of Engineering Mechanics, China Earthquake Administration; Key Laboratory of Earthquake Engineering and Engineering Vibration of China Earthquake Administration, Harbin 150080, China*
2. *School of Civil Engineering and Architecture, Heilongjiang University, Harbin 150080, China*
3. *School of Civil Engineering, Harbin Institute of Technology, Harbin 150090, China*
4. *Department of Civil and Environmental Engineering, University of Nevada, Reno NV 89557, USA*

Abstract: This study proposes a Green's function, an essential representation of water-saturated ground under moving excitation, to simulate ground borne vibration from trains. First, general solutions to the governing equations of poroelastic medium are derived by means of integral transform. Secondly, the transmission and reflection matrix approach is used to formulate the relationship between displacement and stress of the stratified ground, which results in the matrix of the Green's function. Then the Green's function is combined into a train-track-ground model, and is verified by typical examples and a field test. Additional simulations show that the computed ground vibration attenuates faster in the immediate vicinity of the track than in the surrounding area. The wavelength of wheel-rail unevenness has a notable effect on computed displacement and pore pressure. The variation of vibration intensity with the depth of ground is significantly influenced by the layering of the strata soil. When the train speed is equal to the velocity of the Rayleigh wave, the Mach cone appears in the simulated wave field. The proposed Green's function is an appropriate representation for a layered ground with shallow ground water table, and will be helpful to understand the dynamic responses of the ground to complicated moving excitation.

Keywords: wave propagation; poroelastic medium; layered half-space; train; Green's function

1 Introduction

Due to processes of transportation and deposition, a natural ground commonly consists of horizontal layers, beneath which is a firm strata or bedrock. This feature makes the multi-layered half-space (i.e., an underlying half-space overlaid by several horizontal layers, as shown in Fig. 1) an adequate mechanical model for subgrade or ground of engineering structures. Displacement responses of a multi-layered half-space to a unit time-harmonic load acting on the surface are sometimes referred to as the Green's functions in the frequency domain (Sheng *et al*., 1999a, b). For an arbitrarily distributed time-harmonic load on the ground surface, the displacement response can be calculated by the convolution of the Green's function. If the excitation is non-harmonic, the Fourier series method can be employed to decompose the excitation into a number of harmonic components, and the response to each harmonic can be carried out one by one based on the same Green's function, and the total response can be obtained by superposition.

For linear systems, the Green's function based approach plays a fundamental role in dealing with the problem of arbitrarily distributed load, even moving load, and the problem of dynamic interaction between soil and structures. The train-induced ground vibration problem involves both moving excitation and dynamic interaction of train-track-ground systems.

During a train running on a track, there are always complicated interactions between the train, the track and the ground. Coupled vibrations of the three subsystems have been modeled in some past studies (e. g., Sheng *et al*., 2003; 2004; Lombaert *et al*., 2006; Lombaert and Degrande, 2009), in which the soil is commonly simplified to be a single-phase viscoelastic medium governed by Navier's elastodynamic equation, and the

Correspondence to: Wang Futong, School of Civil Engineering and Architecture, Heilongjiang University, Harbin 150080, China
Tel: +8618686834212
E-mail: wang-futong@126.com
†Associate Professor; ‡Professor

Supported by: National Natural Science Foundation of China Key Project, under Grant No. 50538030; Postdoctoral Science Foundation of China under Grant No. 2013M531084 and Natural Science Foundation of Heilongjiang Province of China under Grant No. E201221

Received April 18, 2016; **Accepted** October 18, 2016

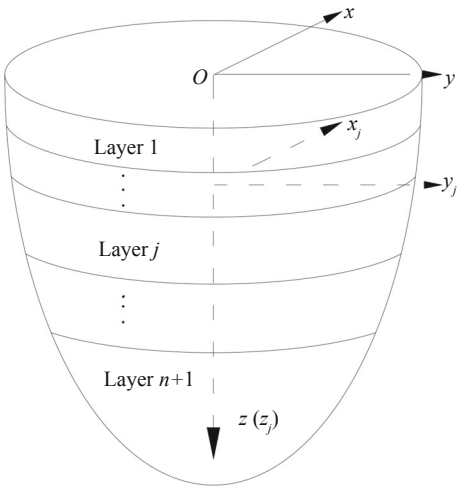

Fig. 1 Layered half-space model for ground

Green's function of ground is derived with the propagator matrix method (Thomson, 1950; Haskell, 1953). By taking account of the compatibility at wheel-rail contacts in a moving Cartesian coordinate system, the wheel-rail forces can be worked out and therefore the ground vibration is obtained. The single-phase continuum based soil model is somewhat straightforward to study the dynamics of ground. However, geotechnical material is more like a multi-phase medium. For water-saturated soil, the relatively incompressible pore water undertakes part of stress transfer, and may also be moving relative to soil skeleton, creating friction between the fluid and the solid phases. In many cases, the influence of the groundwater has been so large that the single-phase model is incapable of producing reasonable results (Beskou and Theodorakopoulos, 2011; Cai *et al*., 2009).

Alternatively, the homogeneous poroelastic half-space has been presented (Jin *et al*., 2004; Lu and Jeng, 2007; Lefeuve-Mesgouez and Mesgouez, 2008; Sun *et al*., 2010; Cao *et al*., 2011) as a more refined model of ground subjected to moving loads. The homogeneous hypothesis has an intrinsic limitation concerning the fact of soil layering, which inhibits the consideration of invariant soil properties along the depth of ground, preventing the application of these models in the study of special wave phenomena such as reflection and refraction at interfaces of soil layers.

Clearly, the multi-layered poroelastic half-space is a more realistic representation of natural ground than the homogeneous one. The origin of theoretical studies on the stratified media, though of single-phase, can be traced back to the propagator matrix method (Thomson, 1950; Haskell, 1953). This approach was often subject to numerical difficulties (overflow) in case of thick layers or very high wave number due to mismatched exponential terms presented in the propagator matrices. Improvements have been achieved (Lowe, 1995; Rokhlin and Wang, 2002; Apsel and Luco, 1983; Luco and Apsel, 1983) by decomposing the wave field into downward transmitting and upward reflected parts, which is commonly known as the transmission and reflection matrix (TRM) method. Theoretical studies on the layered poroelastic media under time-varying moving load can also be found in the literature (Siddharthan *et al*., 1993a, b; Mesgouez and Lefeuve-Mesgouez, 2009; Lefeuve-Mesgouez and Mesgouez, 2012; Lu *et al*., 2009; Xu *et al*., 2007, 2008; Wang *et al*., 2015), but the Green's function were usually not presented explicitly. In the case of non-moving excitation, a dynamic Green's function has been proposed by Zheng *et al*. (2013), where the excitations are buried inside layered media and can be useful in modeling vibration from underground facilities.

The objectives of the this research are to: (1) develop a theoretical dynamic Green's function for multi-layered poroelastic half-space under moving load, (2) incorporate the Green's function into a sophisticated train-track-ground model (Sheng *et al*., 2003, 2004), and (3) simulate train-induced ground vibrations with groundwater effects included.

To this end, the Fourier integral transforms are applied to the three-dimensional Biot's equation to get its exact general solutions, then the TRM approach is used to derive the Green's function for the poroelatstic multi-layered half-space, and thereafter, the derived Green's function is combined into the coupled train-track-ground model. The proposed approach is verified by two typical numerical examples in the literature and observed data from an in situ test. Simulated vertical displacements, excess pore pressures and total stresses are selected to demonstrate the features of ground vibration and the effect of soil layering.

2 Solutions to governing equation of poroelastic medium in Fourier transformed domain

Consider a fluid-saturated poroelastic medium in the Cartesian coordinate system, and let U_i and w_i (i=x,y,z) represent the displacements of the solid skeleton and the infiltration displacements of the pore fluid, respectively. The motions of the two phases can be formulated as (Biot, 1962),

$$\begin{cases} \mu U_{i,jj} + (\lambda_c + \mu) U_{j,ji} + \alpha M w_{j,ji} = \rho \ddot{U}_i + \rho_f \ddot{w}_i \\ \alpha M U_{j,ji} + M w_{j,ji} = \rho_f \ddot{U}_i + m \ddot{w}_i + b \dot{w}_i \end{cases} \tag{1}$$

where ρ and ρ_f denote the mass densities of the bulk material and the fluid; m is a density-like parameter, and $m = \tau\rho_f/\varphi$, with φ the porosity and τ the void tortuosity; b represents the viscous coupling between the solid and the fluid, $b = \gamma_f /k$, with γ_f the unit weight of fluid and k the coefficient of permeability; M and α are known as the first and second Biot's parameters accounting for the relative compressibility of the two phases; and $\lambda_c = \lambda + \alpha^2 M$, λ and μ are the drained Lamé constants for the viscoelastic

porous media. Hysteretic damping of the solid phase can be involved by representing the two Lamé constants as (Lefeuve-Mesgouez and Mesgouez, 2008; Mesgouez and Lefeuve-Mesgouez, 2009; Sheng *et al*., 1999b),

$$\lambda = \lambda_0 [1+2\mathrm{i}\eta \mathrm{sgn}(\omega)] \tag{2a}$$

$$\mu = \mu_0 [1+2\mathrm{i}\eta \mathrm{sgn}(\omega)] \tag{2b}$$

where λ_0 and μ_0 are the two corresponding undamped constants, η is the loss factor and ω is the angular frequency of vibration, respectively.

The constitutive relationships have the form of

$$\begin{cases} \sigma_{ij} = \lambda e\delta_{ij} + \mu(U_{i,j} + U_{j,i}) - \alpha\delta_{ij}P_\mathrm{f} \\ -P_\mathrm{f} = M\varepsilon + \alpha M e \end{cases} \tag{3}$$

where σ_{ij} is the stress tensor of the bulk medium, P_f is the excess pore pressure and δ_{ij} is the Kronecker delta. The volume of fluid flowing out from the unit volume of bulk material is given by $\varepsilon = w_{i,i}$, and the dilatation of the solid skeleton is $e = U_{i,i}$.

In the case of harmonic vibration with an angular frequency of ω, all the displacements, stresses and strains are of the harmonic form, e. g., the displacements are given by,

$$U_i(x,y,z,t) = \tilde{U}_i(x,y,z)\mathrm{e}^{\mathrm{i}\omega t} \tag{4}$$

in which the function with a tilde overhead denotes the complex amplitude of the time-harmonic quantity. Substituting these harmonic expressions into Eq. (1) yields,

$$\begin{cases} \mu\tilde{U}_{i,jj} + (\lambda_\mathrm{c} + \mu)\tilde{U}_{j,ji} + \alpha M\tilde{w}_{j,ji} = -\omega^2(\rho\tilde{U}_i + \rho_\mathrm{f}\tilde{w}_i) \\ \alpha M\tilde{U}_{j,ji} + M\tilde{w}_{j,ji} = -\omega^2\rho_\mathrm{f}\tilde{U}_i - \omega^2 m\tilde{w}_i + \mathrm{i}\omega b\tilde{w}_i \end{cases} \tag{5}$$

Multiplying both sides by gradient operator ∇, the dot products give the equations in terms of volume strain,

$$\begin{cases} (\lambda_\mathrm{c} + 2\mu)\nabla^2\tilde{e} + \alpha M\nabla^2\tilde{\varepsilon} = -\omega^2(\rho\tilde{e} + \rho_\mathrm{f}\tilde{\varepsilon}) \\ \alpha M\nabla^2\tilde{e} + M\nabla^2\tilde{\varepsilon} = -\rho_\mathrm{f}\omega^2\tilde{e} + (\mathrm{i}b\omega - m\omega^2)\tilde{\varepsilon} \end{cases} \tag{6}$$

Applying the Fourier transform pairs

$$\bar{\bar{f}}(\beta,\gamma,z) = \int_{-\infty}^{\infty}\int_{-\infty}^{\infty}\tilde{f}(x,y,z)\mathrm{e}^{-\mathrm{i}(\beta x+\gamma y)}\,\mathrm{d}x\mathrm{d}y \tag{7}$$

$$\tilde{f}(x,y,z) = \frac{1}{(2\pi)^2}\int_{-\infty}^{\infty}\int_{-\infty}^{\infty}\bar{\bar{f}}(\beta,\gamma,z)\mathrm{e}^{\mathrm{i}(\beta x+\gamma y)}\,\mathrm{d}\beta\mathrm{d}\gamma \tag{8}$$

to Eq. (6) to transform from the space domain (x, y) into the angular wave number domain (β, γ) yields,

$$\begin{cases} (\lambda_\mathrm{c} + 2\mu)\bar{\bar{e}}'' + \alpha M\bar{\bar{\varepsilon}}'' + [\omega^2\rho - r^2(\lambda_\mathrm{c} + 2\mu)]\bar{\bar{e}} + (\omega^2\rho_\mathrm{f} - r^2\alpha M)\bar{\bar{\varepsilon}} = 0 \\ \alpha M\bar{\bar{e}}'' + M\bar{\bar{\varepsilon}}'' + (\omega^2\rho_\mathrm{f} - r^2\alpha M)\bar{\bar{e}} - (\mathrm{i}b\omega - m\omega^2 + Mr^2)\bar{\bar{\varepsilon}} = 0 \end{cases} \tag{9}$$

in which the double prime stands for the second derivative with respect to z, and $r^2 = \beta^2 + \gamma^2$. Equation (9) is a homogeneous second-order linear ordinary differential equation of dilatations. The general solution can be written as,

$$\begin{cases} \bar{\bar{e}} = A_1(\xi_{\mathrm{p}1}^2 - \xi^2)\mathrm{e}^{-\xi_{\mathrm{p}1}z} + B_1(\xi_{\mathrm{p}1}^2 - \xi^2)\mathrm{e}^{\xi_{\mathrm{p}1}z} \\ \quad + A_2(\xi_{\mathrm{p}2}^2 - \xi^2)\mathrm{e}^{-\xi_{\mathrm{p}2}z} + B_2(\xi_{\mathrm{p}2}^2 - \xi^2)\mathrm{e}^{\xi_{\mathrm{p}2}z} \\ \bar{\bar{\varepsilon}} = A_1d_1(\xi_{\mathrm{p}1}^2 - \xi^2)\mathrm{e}^{-\xi_{\mathrm{p}1}z} + B_1d_1(\xi_{\mathrm{p}1}^2 - \xi^2)\mathrm{e}^{\xi_{\mathrm{p}1}z} \\ \quad + A_2d_2(\xi_{\mathrm{p}2}^2 - \xi^2)\mathrm{e}^{-\xi_{\mathrm{p}2}z} + B_2d_2(\xi_{\mathrm{p}2}^2 - \xi^2)\mathrm{e}^{\xi_{\mathrm{p}2}z} \end{cases} \tag{10}$$

where A_1, B_1, A_2 and B_2 are arbitrary functions depending on boundary conditions, and

$$\xi = \sqrt{r^2 - \omega^2/V_\mathrm{s}^2} \tag{11}$$

$$\xi_{\mathrm{p}i} = \sqrt{r^2 - \omega^2/V_{\mathrm{p}i}^2}, \qquad i = 1,2 \tag{12}$$

Here $V_{\mathrm{p}1}$, $V_{\mathrm{p}2}$ and V_s are the phase velocities of P1, P2 and S waves of the poroelastic medium, and can be obtained by solving the equations

$$\frac{1}{V_\mathrm{s}^2} = \frac{\rho}{\mu} + \frac{\rho_\mathrm{f}^2}{(\mathrm{i}b/\omega - m)\mu} \tag{13}$$

and

$$\begin{cases} \dfrac{1}{V_{\mathrm{p}1}^2}\cdot\dfrac{1}{V_{\mathrm{p}2}^2} = \dfrac{(m - \mathrm{i}b/\omega)\rho - \rho_\mathrm{f}^2}{M(\lambda + 2\mu)} \\ \dfrac{1}{V_{\mathrm{p}1}^2} + \dfrac{1}{V_{\mathrm{p}2}^2} = \dfrac{(m - \mathrm{i}b/\omega)(\lambda_\mathrm{c} + 2\mu)}{M(\lambda + 2\mu)} + \dfrac{\rho - 2\alpha\rho_\mathrm{f}}{\lambda + 2\mu} \end{cases} \tag{14}$$

Note that the P1 wave always propagates faster than the P2 wave, so the complex values of $V_{\mathrm{p}1}$ and $V_{\mathrm{p}2}$ obtained by Eq. (14) should always be chosen to guarantee the inequality $\mathrm{Re}(V_{\mathrm{p}1}) > \mathrm{Re}(V_{\mathrm{p}2})$. It is also worth noticing in Eqs. (13, 14) that in the case of $b \neq 0$ (or $k \neq \infty$), all velocities of the three kinds of waves are frequency-dependent, i.e., body waves in the two-phase medium are of frequency dispersion except in the extreme condition of totally free flowing.

By applying the Fourier transform of Eq. (7) on Eq. (5) and introducing the volume strain solutions of Eq. (10), the displacement solutions are derived as follows,

$$
\begin{cases}
\bar{\tilde{w}}_z = -\dfrac{t_1\xi_{\mathrm{p}1}}{b_0}B_1\mathrm{e}^{\xi_{\mathrm{p}1}z} - \dfrac{\xi_{\mathrm{p}2}t_2}{b_0}B_2\mathrm{e}^{\xi_{\mathrm{p}2}z} - \dfrac{\mathrm{i}\beta}{\xi b_0}\rho_{\mathrm{f}}B_3\mathrm{e}^{\xi z} - \\
\qquad \dfrac{\mathrm{i}\gamma}{\xi b_0}\rho_{\mathrm{f}}B_4\mathrm{e}^{\xi z} + \dfrac{t_1\xi_{\mathrm{p}1}}{b_0}A_1\mathrm{e}^{-\xi_{\mathrm{p}1}z} + \dfrac{\xi_{\mathrm{p}2}t_2}{b_0}A_2\mathrm{e}^{-\xi_{\mathrm{p}2}z} + \\
\qquad \dfrac{\mathrm{i}\beta}{\xi b_0}\rho_{\mathrm{f}}A_3\mathrm{e}^{-\xi z} + \dfrac{\mathrm{i}\gamma}{\xi b_0}\rho_{\mathrm{f}}A_4\mathrm{e}^{-\xi z} \\
\bar{\tilde{U}}_x = -\mathrm{i}\beta g_1 B_1\mathrm{e}^{\xi_{\mathrm{p}1}z} - \mathrm{i}\beta g_2 B_2\mathrm{e}^{\xi_{\mathrm{p}2}z} + B_3\mathrm{e}^{\xi z} - \\
\qquad \mathrm{i}\beta g_1 A_1\mathrm{e}^{-\xi_{\mathrm{p}1}z} - \mathrm{i}\beta g_2 A_2\mathrm{e}^{-\xi_{\mathrm{p}2}z} + A_3\mathrm{e}^{-\xi z} \\
\bar{\tilde{U}}_y = -\mathrm{i}\gamma g_1 B_1\mathrm{e}^{\xi_{\mathrm{p}1}z} - \mathrm{i}\gamma g_2 B_2\mathrm{e}^{\xi_{\mathrm{p}2}z} + B_4\mathrm{e}^{\xi z} - \\
\qquad \mathrm{i}\gamma g_1 A_1\mathrm{e}^{-\xi_{\mathrm{p}1}z} - \mathrm{i}\gamma g_2 A_2\mathrm{e}^{-\xi_{\mathrm{p}2}z} + A_4\mathrm{e}^{-\xi z} \\
\bar{\tilde{U}}_z = -\xi_{\mathrm{p}1}g_1 B_1\mathrm{e}^{\xi_{\mathrm{p}1}z} - \xi_{\mathrm{p}2}g_2 B_2\mathrm{e}^{\xi_{\mathrm{p}2}z} - \dfrac{\mathrm{i}\beta}{\xi}B_3\mathrm{e}^{\xi z} - \\
\qquad \dfrac{\mathrm{i}\gamma}{\xi}B_4\mathrm{e}^{\xi z} + \xi_{\mathrm{p}1}g_1 A_1\mathrm{e}^{-\xi_{\mathrm{p}1}z} + \xi_{\mathrm{p}2}g_2 A_2\mathrm{e}^{-\xi_{\mathrm{p}2}z} + \\
\qquad \dfrac{\mathrm{i}\beta}{\xi}A_3\mathrm{e}^{-\xi z} + \dfrac{\mathrm{i}\gamma}{\xi}A_4\mathrm{e}^{-\xi z}
\end{cases} \tag{15}
$$

where A_3, B_3, A_4 and B_4 are the other four arbitrary functions. Considering the constitutive relationships of Eq. (3), all stress components can then be obtained as,

$$
\begin{cases}
\bar{\tilde{P}}_{\mathrm{f}} = -t_{\mathrm{b}1}B_1\mathrm{e}^{\xi_{\mathrm{p}1}z} - t_{\mathrm{b}2}B_2\mathrm{e}^{\xi_{\mathrm{p}2}z} - t_{\mathrm{b}1}A_1\mathrm{e}^{-\xi_{\mathrm{p}1}z} - t_{\mathrm{b}2}A_2\mathrm{e}^{-\xi_{\mathrm{p}2}z} \\
\bar{\tilde{\sigma}}_{xz} = -2\mathrm{i}\mu\beta g_1\xi_{\mathrm{p}1}B_1\mathrm{e}^{\xi_{\mathrm{p}1}z} - 2\mathrm{i}\mu\beta g_2\xi_{\mathrm{p}2}B_2\mathrm{e}^{\xi_{\mathrm{p}2}z} + \\
\qquad \mu(\xi + \dfrac{\beta^2}{\xi})B_3\mathrm{e}^{\xi z} + \dfrac{\mu\beta\gamma}{\xi}B_4\mathrm{e}^{\xi z} + 2\mathrm{i}\mu\beta g_1\xi_{\mathrm{p}1}A_1\mathrm{e}^{-\xi_{\mathrm{p}1}z} + \\
\qquad 2\mathrm{i}\mu\beta g_2\xi_{\mathrm{p}2}A_2\mathrm{e}^{-\xi_{\mathrm{p}2}z} - \mu(\xi + \dfrac{\beta^2}{\xi})A_3\mathrm{e}^{-\xi z} - \dfrac{\mu\beta\gamma}{\xi}A_4\mathrm{e}^{-\xi z} \\
\bar{\tilde{\sigma}}_{yz} = -2\mathrm{i}\mu\gamma g_1\xi_{\mathrm{p}1}B_1\mathrm{e}^{\xi_{\mathrm{p}1}z} - 2\mathrm{i}\mu\gamma g_2\xi_{\mathrm{p}2}B_2\mathrm{e}^{\xi_{\mathrm{p}2}z} + \\
\qquad \dfrac{\mu\gamma\beta}{\xi}B_3\mathrm{e}^{\xi z} + \mu(\xi + \dfrac{\gamma^2}{\xi})B_4\mathrm{e}^{\xi z} + 2\mathrm{i}\mu\gamma g_1\xi_{\mathrm{p}1}A_1\mathrm{e}^{-\xi_{\mathrm{p}1}z} + \\
\qquad 2\mathrm{i}\mu\gamma g_2\xi_{\mathrm{p}2}A_2\mathrm{e}^{-\xi_{\mathrm{p}2}z} - \dfrac{\mu\gamma\beta}{\xi}A_3\mathrm{e}^{-\xi z} - \mu(\xi + \dfrac{\gamma^2}{\xi})A_4\mathrm{e}^{-\xi z} \\
\tilde{\sigma}_{zz} = t_{\mathrm{c}1}B_1\mathrm{e}^{\xi_{\mathrm{p}1}z} + t_{\mathrm{c}2}B_2\mathrm{e}^{\xi_{\mathrm{p}2}z} - 2\mu\mathrm{i}\beta B_3\mathrm{e}^{\xi z} - 2\mu\mathrm{i}\gamma B_4\mathrm{e}^{\xi z} + \\
\qquad t_{\mathrm{c}1}A_1\mathrm{e}^{-\xi_{\mathrm{p}1}z} + t_{\mathrm{c}2}A_2\mathrm{e}^{-\xi_{\mathrm{p}2}z} - 2\mu\mathrm{i}\beta A_3\mathrm{e}^{-\xi z} - 2\mu\mathrm{i}\gamma A_4\mathrm{e}^{-\xi z}
\end{cases} \tag{16}
$$

The displacements in Eq. (15) and stresses in Eq. (16) may be written as the combined form of matrix,

$$
\begin{pmatrix} \boldsymbol{u} \\ \boldsymbol{\sigma} \end{pmatrix} = \begin{bmatrix} \boldsymbol{C}_{\mathrm{u}+} & \boldsymbol{C}_{\mathrm{u}-} \\ \boldsymbol{C}_{\sigma+} & \boldsymbol{C}_{\sigma-} \end{bmatrix} \begin{bmatrix} \boldsymbol{E}_{+} & 0 \\ 0 & \boldsymbol{E}_{-} \end{bmatrix} \begin{pmatrix} \boldsymbol{B} \\ \boldsymbol{A} \end{pmatrix} \tag{17}
$$

where the displacement vector $\boldsymbol{u} = \{\bar{\tilde{w}}_z, \bar{\tilde{U}}_x, \bar{\tilde{U}}_y, \bar{\tilde{U}}_z\}^{\mathrm{T}}$, stress vector $\boldsymbol{\sigma} = \{\bar{\tilde{P}}_{\mathrm{f}}, \bar{\tilde{\sigma}}_{xz}, \bar{\tilde{\sigma}}_{yz}, \bar{\tilde{\sigma}}_{zz}\}^{\mathrm{T}}$, arbitrary function vector $\boldsymbol{B} = \{B_1, B_2, B_3, B_4\}^{\mathrm{T}}$ and $\boldsymbol{A} = \{A_1, A_2, A_3, A_4\}^{\mathrm{T}}$, positive exponent matrix $\boldsymbol{E}_{+} = \mathrm{diag}(\mathrm{e}^{\xi_{\mathrm{p}1}z}, \mathrm{e}^{\xi_{\mathrm{p}2}z}, \mathrm{e}^{\xi z}, \mathrm{e}^{\xi z})$, and negative exponent matrix $\boldsymbol{E}_{-} = (\boldsymbol{E}_{+})^{-1} = \mathrm{diag}(\mathrm{e}^{-\xi_{\mathrm{p}1}z}, \mathrm{e}^{-\xi_{\mathrm{p}2}z}, \mathrm{e}^{-\xi z}, \mathrm{e}^{-\xi z})$. The parameters d_1, d_2, t_1, t_2, g_1, g_2, b_0, b_1, b_2, $t_{\mathrm{b}1}$, $t_{\mathrm{b}2}$, $t_{\mathrm{c}1}$ and $t_{\mathrm{c}2}$ in Eqs. (10)–(17), and the elements in the matrices of $\boldsymbol{C}_{\mathrm{u}+}$, $\boldsymbol{C}_{\mathrm{u}-}$ $\boldsymbol{C}_{\sigma+}$ and $\boldsymbol{C}_{\sigma-}$ are detailed in the Appendix. On the right side of Eq. (17), the exponent matrices $\boldsymbol{E}_{-}$ and $\boldsymbol{E}_{+}$ depend on the vertical coordinate z, while other terms are independent of z.

3 Formulation of the Green's function matrix

The n layers in Fig. 1 are numbered successively from top to bottom, with the special (n+1)th 'layer' representing the underlying half-space. The thickness of the jth layer is denoted by $h^{(j)}$, and for the underlying half-space, $h^{(n+1)}=\infty$. All layers and the underlying half-space are of poroelastic materials. Within each layer the properties are homogeneous, and defined by a set of material parameters. Each layer has a local Cartesian coordinate system with the origin located on its top, and the *oxyz* stands for a global coordinate system with the origin on the top surface of the first layer. In the local coordinate system, the vertical location $z^{(j)}=0$ for the upper face, and $z^{(j)}= h^{(j)}$ for the lower face of the layer. Introducing the superscript j to the quantities, Eq. (17) can be rewritten for each of the layers,

$$
\begin{pmatrix} \boldsymbol{u}^j \\ \boldsymbol{\sigma}^j \end{pmatrix} = \begin{bmatrix} \mathbf{C}^j_{u+} & \mathbf{C}^j_{u-} \\ \mathbf{C}^j_{\sigma+} & \mathbf{C}^j_{\sigma-} \end{bmatrix} \begin{bmatrix} \mathbf{E}^j_{+} & 0 \\ 0 & \mathbf{E}^j_{-} \end{bmatrix} \begin{pmatrix} \mathbf{B}^j \\ \mathbf{A}^j \end{pmatrix} \quad j = 1, n+1 \tag{18}
$$

Because at the ground surface $z^{(1)} = 0$, $\boldsymbol{E}^j_{+}$ and $\boldsymbol{E}^j_{-}$ become identity matrices, and therefore,

$$
\begin{pmatrix} \boldsymbol{u}^1_0 \\ \boldsymbol{\sigma}^1_0 \end{pmatrix} = \begin{bmatrix} \boldsymbol{C}^1_{u+} & \boldsymbol{C}^1_{u-} \\ \boldsymbol{C}^1_{\sigma+} & \boldsymbol{C}^1_{\sigma-} \end{bmatrix} \begin{pmatrix} \boldsymbol{B}^1 \\ \boldsymbol{A}^1 \end{pmatrix} \tag{19}
$$

where $\boldsymbol{u}^1_0$ and $\boldsymbol{\sigma}^1_0$ denote the displacement and stress vector of the ground surface.

At the interface of the jth and the (j+1)th layers, the displacements and stresses of the upper layer equal those of the lower layer. This condition can be written in terms of Eq. (18) as,

$$
\begin{bmatrix} \boldsymbol{C}^{j+1}_{u+} & \boldsymbol{C}^{j+1}_{u-} \\ \boldsymbol{C}^{j+1}_{\sigma+} & \boldsymbol{C}^{j+1}_{\sigma-} \end{bmatrix} \begin{pmatrix} \boldsymbol{B}^{j+1} \\ \boldsymbol{A}^{j+1} \end{pmatrix} = \begin{bmatrix} \boldsymbol{C}^j_{u+} & \boldsymbol{C}^j_{u-} \\ \boldsymbol{C}^j_{\sigma+} & \boldsymbol{C}^j_{\sigma-} \end{bmatrix} \begin{bmatrix} \boldsymbol{E}^j_{+,h} & 0 \\ 0 & \boldsymbol{E}^j_{-,h} \end{bmatrix} \begin{pmatrix} \boldsymbol{B}^j \\ \boldsymbol{A}^j \end{pmatrix}, j = 1, n, \tag{20}
$$

where $\boldsymbol{E}^j_{+,h}$ and $\boldsymbol{E}^j_{-,h}$ denote the exponent matrices $\boldsymbol{E}^j_{+}$ and $\boldsymbol{E}^j_{-}$ at the bottom of jth layer, respectively. Eq. (20) can be rewritten as,

$$
\begin{pmatrix} \boldsymbol{B}^{j+1} \\ \boldsymbol{A}^{j+1} \end{pmatrix} = \begin{bmatrix} \boldsymbol{T}^j_{11} & \boldsymbol{T}^j_{12} \\ \boldsymbol{T}^j_{21} & \boldsymbol{T}^j_{22} \end{bmatrix} \begin{bmatrix} \boldsymbol{E}^j_{+,h} & 0 \\ 0 & \boldsymbol{E}^j_{-,h} \end{bmatrix} \begin{pmatrix} \boldsymbol{B}^j \\ \boldsymbol{A}^j \end{pmatrix}, j = 1, n \tag{21}
$$

in which the 8 × 8 matrix,

$$\begin{bmatrix} \boldsymbol{T}_{11}^{j} & \boldsymbol{T}_{12}^{j} \\ \boldsymbol{T}_{21}^{j} & \boldsymbol{T}_{22}^{j} \end{bmatrix} = \begin{bmatrix} \boldsymbol{C}_{u+}^{j+1} & \boldsymbol{C}_{u-}^{j+1} \\ \boldsymbol{C}_{\sigma+}^{j+1} & \boldsymbol{C}_{\sigma-}^{j+1} \end{bmatrix}^{-1} \begin{bmatrix} \boldsymbol{C}_{u+}^{j} & \boldsymbol{C}_{u-}^{j} \\ \boldsymbol{C}_{\sigma+}^{j} & \boldsymbol{C}_{\sigma-}^{j} \end{bmatrix}, \ j=1, n \quad (22)$$

Introducing a matrix $\boldsymbol{R}^j$ to represent the relationship between the vectors $\boldsymbol{B}^j$ and $\boldsymbol{A}^j$, i.e.,

$$\boldsymbol{B}^j = \boldsymbol{R}^j \boldsymbol{A}^j \quad (23)$$

and substituting the relationship of Eq. (23) into Eq. (21) yields,

$$\boldsymbol{R}^j = -\boldsymbol{E}_{-,h}^{j}(\boldsymbol{T}_{11}^{j} - \boldsymbol{R}^{j+1}\boldsymbol{T}_{21}^{j})^{-1}(\boldsymbol{T}_{12}^{j} - \boldsymbol{R}^{j+1}\boldsymbol{T}_{22}^{j})\boldsymbol{E}_{-,h}^{j}, \quad j=1, n \quad (24a)$$

In the case of the underlying half-space, the displacements in Eq. (15) and (16) must approach 0 while z goes to infinity. It can therefore be concluded that any coefficients of positive exponent terms must equal zero, i.e., $\boldsymbol{B}^{n+1}$ must be a zero vector. As a result, Eq. (23) of the underlying half-space becomes $\boldsymbol{R}^{n+1}\boldsymbol{A}^{n+1}=0$. Since the displacements and stresses in the underlying half-space cannot be all zeros, $\boldsymbol{A}^{n+1}$ must not be a zero vector, which indicates that,

$$\boldsymbol{R}^{n+1} = 0 \quad (24b)$$

must hold.

Equtions (24a, b) have formulated an iterative procedure for calculating the matrix $\boldsymbol{R}^j$ from the underlying half-space to the first layer.

Substituting the expression $\boldsymbol{B}^1 = \boldsymbol{R}^1\boldsymbol{A}^1$ into Eq. (19) gives,

$$\boldsymbol{u}_0^1 = \boldsymbol{\delta}\boldsymbol{\sigma}_0^1 \quad (25)$$

in which the matrix

$$\boldsymbol{\delta} = (\boldsymbol{C}_{u+}^{1}\boldsymbol{R}^1 + \boldsymbol{C}_{u-}^{1})(\boldsymbol{C}_{\sigma+}^{1}\boldsymbol{R}^1 + \boldsymbol{C}_{\sigma-}^{1})^{-1} \quad (26)$$

relates the stresses $\boldsymbol{\sigma}_0^1$ to the displacements $\boldsymbol{u}_0^1$ of the ground surface, and is termed as the dynamic receptance matrix, or the Green's function matrix in the transformed domain.

The vertical vibration of ground surface is commonly the predominant component; therefore, in most cases of modeling ground vibration from trains (e.g. Sheng *et al.*, 1999a, b, 2003, 2004; Lombaert and Degrande, 2009; Lombaert *et al.,* 2006), only the vertical excitation needs to be taken into account, and the effect of the two shear stresses on the ground surface can be neglected. Then for the permeable ground surface, $\bar{\bar{P}}_f = \bar{\bar{\sigma}}_{xz} = \bar{\bar{\sigma}}_{yz} = 0$, i.e., $\boldsymbol{\sigma}_0^1=(0,0,0,\bar{\bar{\sigma}}_{zz})^{\mathrm{T}}$ in Eq. (25). Thus, the vertical displacement,

$$\bar{\bar{U}}_z(\beta,\gamma,0,\omega) = \bar{\bar{\delta}}_{44}(\beta,\gamma,\omega)\bar{\bar{\sigma}}_{zz}(\beta,\gamma,0,\omega) \quad (27)$$

Applying the inverse Fourier transform defined in Eq. (8) to Eq. (27) yields the following convolution,

$$\tilde{U}_z(x,y,0,\omega) = \int_{-\infty}^{+\infty}\int_{-\infty}^{+\infty} \tilde{\delta}_{44}(x-r,y-s,\omega)\tilde{\sigma}_{zz}(r,s,0,\omega)\mathrm{d}r\mathrm{d}s \quad (28)$$

where $\tilde{U}_z(x,y,z,\omega)$, $\tilde{\delta}_{44}(x,y,\omega)$ and $\tilde{\sigma}_{zz}(x,y,z,\omega)$ are the inverse transforms, respectively, of $\bar{\bar{U}}_z(\beta,\gamma,z,\omega)$, $\bar{\bar{\delta}}_{44}(\beta,\gamma,\omega)$ and $\bar{\bar{\sigma}}_{zz}(\beta,\gamma,z,\omega)$. According to the physical meaning of the convolution, $\tilde{\delta}_{44}(x,y,\omega)$ is the amplitude of the vertical displacement response at the point (x,y) to a vertical harmonic excitation $e^{i\omega t}$ acting at the origin, which indicates that $\tilde{\delta}_{44}(x,y,\omega)$ is the vertical displacement Green's function in the frequency-space domain, and $\bar{\bar{\delta}}_{44}(\beta,\gamma,\omega)$ represents its transform in the frequency-wave number domain.

If the harmonic load with an angular frequency Ω_k moves along the x axis with a speed c, the single frequency of the load may excite infinite frequency contents of the ground vibration. The relationship between the frequency of excitation and the frequency of ground vibration ω can be written as (Sheng *et al.* 1999b),

$$\omega = \Omega_k - \beta c \quad (29)$$

Substituting Eq. (29) to Eq. (26) results in the Green's functions for moving load. In this case, the inverse Fourier transform of the Green's function with respect to (β, γ) is the complex amplitude of the ground vibration in a coordinate system (x_*, y) traveling together with the load, where the moving coordinate $x_* = x - ct$.

In summary, the implementation of calculating the Green's function is as follows:

- calculate every layers' coefficient matrices $\boldsymbol{C}_{u+}^{j}$, $\boldsymbol{C}_{u-}^{j}$, $\boldsymbol{C}_{\sigma+}^{j}$, $\boldsymbol{C}_{\sigma-}^{j}$ and exponent matrix $\boldsymbol{E}_{-,h}^{j}$ in terms of their specific expressions listed in the Appendix;
- carry out all interface matrices $\boldsymbol{T}_{11}^{j}$, $\boldsymbol{T}_{12}^{j}$, $\boldsymbol{T}_{21}^{j}$ and $\boldsymbol{T}_{22}^{j}$ according to Eq. (22);
- iteratively calculate each layer's matrix $\boldsymbol{R}^j$ according to Eq. (24) from bottom to top;
- calculate the Green's function matrix $\boldsymbol{\delta}$ in terms of Eq. (26).

In dealing with moving excitations, the frequency ω should be replaced by $\Omega_k - \beta c$ as Eq. (29).

4 Model of train-track-ground coupled vibration

Figure 2 illustrates the mechanical model of the train, the track and the ground (Sheng *et al.* 2003, 2004). The train is simplified as a mass-spring-dashpot system, with the mass matrix being $\boldsymbol{M}_T$ and complex stiffness matrix $\boldsymbol{K}_T$. The track is infinitely long in the x direction, and has a contact width of $2b_t$ with the ground. The rails are modeled as an infinitely long Euler beam, of which the mass per unit length is m_R, and the flexural rigidity is EI. The sleepers are modeled by a distributed mass along the track direction x, with the mass per unit

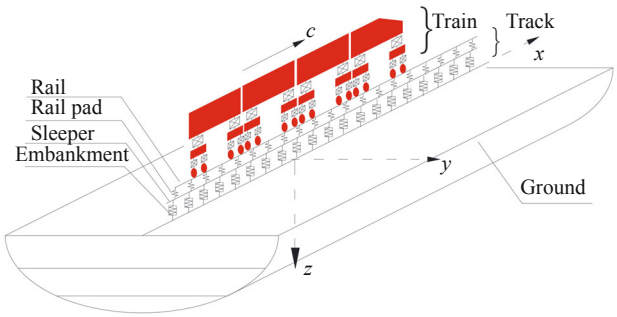

Fig. 2 The coupled train-track-ground system

length being m_s. The rail pads are approximated by a continuous spring distributed along the x direction, with the spring stiffness k_p. The embankment is simplified by means of consistent mass approximation with a mass per unit length m_B, and only the vertical stiffness k_B is taken into account. Material damping effects of all track components are formulated similar to Eq. (2), and EI, k_B and k_p are all complex numbers with loss factors in their imaginary parts. For the train and the track, only the vertical dynamics are considered. The interactive stress between the embankment and the ground is assumed to be vertical and uniformly distributed along the y direction.

The first step of modeling is to calculate the response of the track-ground subsystem excited by a time-harmonic load $e^{i\Omega_k t}$ moving on the track with the train speed c. The governing equations for the rail beam, sleeper mass and the embankment are as follows (Sheng *et al.,* 1999b),

$$EI\beta^4\bar{\bar{w}}_1(\beta)-(\Omega_k-\beta c)^2 m_R\bar{\bar{w}}_1(\beta)+k_p\left[\bar{\bar{w}}_1(\beta)-\bar{\bar{w}}_2(\beta)\right]=1 \tag{30a}$$

$$-(\Omega_k-\beta c)^2 m_s\bar{\bar{w}}_2(\beta)+k_p\left[\bar{\bar{w}}_2(\beta)-\bar{\bar{w}}_1(\beta)\right]=-\bar{\bar{F}}_2(\beta) \tag{30b}$$

$$-\frac{m_B(\Omega_k-\beta c)^2}{6}\begin{bmatrix}2 & 1\\ 1 & 2\end{bmatrix}\begin{Bmatrix}\bar{\bar{w}}_2(\beta)\\ \bar{\bar{w}}_3(\beta)\end{Bmatrix}+ k_B\begin{bmatrix}1 & -1\\ -1 & 1\end{bmatrix}\begin{Bmatrix}\bar{\bar{w}}_2(\beta)\\ \bar{\bar{w}}_3(\beta)\end{Bmatrix}=\begin{Bmatrix}\bar{\bar{F}}_2(\beta)\\ -\bar{\bar{F}}_3(\beta)\end{Bmatrix} \tag{30c}$$

The displacement continuity at the interface of the embankment and the ground can be written as,

$$\bar{\bar{w}}_3(\beta)=\frac{1}{2\pi}\int_{-\infty}^{+\infty}\bar{\bar{U}}_z(\beta,\gamma,z=0,\Omega_k-\beta c)\mathrm{d}\gamma \tag{30d}$$

and the continuity of the stress is,

$$\bar{\bar{\sigma}}_{zz}(\beta,\gamma,0,\Omega_k-\beta c)=-\bar{\bar{F}}_3(\beta)\frac{\sin\gamma b_t}{\gamma b_t} \tag{30e}$$

There are seven unknown functions to be determined in the six equations above, where w_1 is the vertical displacement of the rail, w_2 is the displacement of the sleeper, w_3 is the displacement of the embankment's bottom, F_2 is the interactive force between sleeper and embankment, F_3 is the interactive force between embankment and ground, U_z is the vertical displacement of ground surface, and σ_{zz} is the vertical stress on the ground, respectively. Equation (27) describes the relationship between U_z and σ_{zz}, which is the needed seventh equation, so that the seven unknowns can be determined.

Multiplying the obtained stress solution $\boldsymbol{\sigma}_0^1=(0,0,0,\bar{\bar{\sigma}}_{zz})^T$ to the Green's function matrix $\boldsymbol{\delta}$ in terms of Eq. (25) results in the displacement vector of the ground surface $\boldsymbol{u}_0^1$, then the arbitrary functions $\boldsymbol{A}^1$ and $\boldsymbol{B}^1$ for the first layer can be obtained by solving Eq. (19). Other arbitrary functions $\boldsymbol{A}^j$ and $\boldsymbol{B}^j$, j=2, n+1, can be determined successively by using Eq. (21). The responses $\boldsymbol{u}=\{\bar{\bar{w}}_z,\bar{\bar{U}}_x,\bar{\bar{U}}_y,\bar{\bar{U}}_z\}^T$ and $\boldsymbol{\sigma}=\{\bar{\bar{P}}_f,\bar{\bar{\sigma}}_{xz},\bar{\bar{\sigma}}_{yz},\bar{\bar{\sigma}}_{zz}\}^T$ at any depth of the ground can be calculated according to Eq. (18). The inverse Fourier transform of the solutions in the wave number domain yields their complex amplitudes in the moving space domain (x_*,y,z); e.g., the inverse transforms of rail displacement $\bar{\bar{w}}_1(\beta)$ and ground displacement $\tilde{\bar{U}}_z(\beta,\gamma,z)$ are $\tilde{w}_1(x_*)$ and $\tilde{U}_z(x_*,y,z)$, respectively.

The second step of modeling the train-induced ground vibration is to derive the wheel-rail forces under the condition of harmonic wheel-rail unevenness (Sheng *et al.,* 2004). In this case, the vertical location of the wheel-rail contact point is harmonically varying with the x-coordinate, and the spatial wavelength of the unevenness is $\lambda_k=2\pi c/\Omega_k$. Thus the axles must oscillate up and down in a time-harmonic way with the frequency being $\Omega_k/2\pi$ when the train is travelling at the speed of c. The harmonic motions of the axles result in a series of time-harmonic forces acting on all the wheel-rail contacts moving along the track. If the initial location of the lth and mth wheelsets are $x=a_l$ and $x=a_m$ at the time $t=0$, the horizontal distance of the two points is (a_l-a_m), and $\tilde{w}_1(a_l-a_m)$ is the transfer function of the track-ground subsystem between the two wheel-rail contact points. All transfer functions of every two wheel-rail contact point constitute a matrix $\boldsymbol{H}_R$, in which the element of the lth row and mth column is given by,

$$H_{lm}^R=\tilde{w}_1(a_l-a_m),\ l,m=1,M, \tag{31}$$

and M is the total number of axles of the train. Thus, the vertical displacements of rail can be written as,

$$\tilde{\boldsymbol{Z}}_R=\boldsymbol{H}_R\tilde{\boldsymbol{P}} \tag{32a}$$

in which the vector $\tilde{\boldsymbol{Z}}_R=\{\tilde{z}_{R1},\tilde{z}_{R2},...,\tilde{z}_{RM}\}^T$ collects the displacement amplitudes of the rail at all wheel-rail contact points; $\tilde{\boldsymbol{P}}=\{\tilde{P}_1,\tilde{P}_2,...,\tilde{P}_M\}^T$ denotes the amplitudes of the wheel-rail dynamic forces.

The motion equation of the train is given in the

frequency domain as,

$$-\Omega_k^2 \boldsymbol{M}_{\mathrm{T}} \tilde{\boldsymbol{Z}}_{\mathrm{T}} + \boldsymbol{K}_{\mathrm{T}} \tilde{\boldsymbol{Z}}_{\mathrm{T}} = -\boldsymbol{B}\tilde{\boldsymbol{P}} \tag{32b}$$

where $\tilde{\boldsymbol{Z}}_{\mathrm{T}} = \{\tilde{z}_{\mathrm{T}1}, \tilde{z}_{\mathrm{T}2}, ..., \tilde{z}_{\mathrm{T}N}\}^{\mathrm{T}}$ collects the displacements and rotations at all the degrees of freedom N of the train model; $\boldsymbol{B}$ is a matrix for transforming degrees of freedom, and $\boldsymbol{B}^{\mathrm{T}}=[\boldsymbol{0}, \boldsymbol{I}]_{M\times N}$, $\boldsymbol{I}$ is a M-dimension identity matrix. The displacements of the axles constitute a sub vector of the displacement vector for all degrees of freedom, i.e.,

$$\tilde{\boldsymbol{Z}}_{\mathrm{w}} = \boldsymbol{B}^{\mathrm{T}} \tilde{\boldsymbol{Z}}_{\mathrm{T}} \tag{32c}$$

Each vertical displacement of axle in $\tilde{\boldsymbol{Z}}_{\mathrm{w}}$ is composed of three parts, which are the deformation of the wheel-rail contact, the uneven vertical location of the contact (wheel-rail unevenness), and the vertical displacement of the rail, i.e.,

$$\tilde{\boldsymbol{Z}}_{\mathrm{w}} = \boldsymbol{K}_{\mathrm{h}}^{-1} \tilde{\boldsymbol{P}} + \tilde{\boldsymbol{Z}} + \tilde{\boldsymbol{Z}}_{\mathrm{R}} \tag{32d}$$

in which $\boldsymbol{K}_{\mathrm{h}}^{-1}\tilde{\boldsymbol{P}}$ represents the deformation of wheel-rail contact, with the matrix $\boldsymbol{K}_{\mathrm{h}}$=diag[$k_{\mathrm{h}1}$, $k_{\mathrm{h}2}$,…, $k_{\mathrm{h}M}$], $k_{\mathrm{h}l}$ the stiffness of linearized Hertz spring between the rail and the lth wheelset; the vector $\tilde{\boldsymbol{Z}}(\Omega_k)$ ={ $\mathrm{e}^{\mathrm{i}\Omega_k a_1/c}$, $\mathrm{e}^{\mathrm{i}\Omega_k a_2/c}$,…, $\mathrm{e}^{\mathrm{i}\Omega_k a_M/c}$ }$^{\mathrm{T}}$ collects the wheel-rail unevenness perceived by all the wheels.

After some simple manipulations of Eq. (32), the wheel-rail force vector can be solved as,

$$\tilde{\boldsymbol{P}} = -\left[\boldsymbol{H}_{\mathrm{R}} + \boldsymbol{H}_{\mathrm{w}} + \boldsymbol{K}_{\mathrm{h}}^{-1}\right]^{-1} \tilde{\boldsymbol{Z}} \tag{33}$$

The final step of the modeling is to calculate the ground vibration caused by the wheel-rail forces and by random wheel-rail uneven contact. Ground responses under condition of the harmonic wheel-rail unevenness can be obtained by superimposing the responses to moving harmonic loads with the wheel-rail forces in Eq. (33) being weighting factors, e.g., the vertical displacement amplitude of ground in the moving reference of coordinate,

$$\tilde{U}_{z,\mathrm{P}}(x_*, y, z) = \sum_{l=1}^{M} \tilde{U}_z(x_* - a_l, y, z)\tilde{P}_l(\Omega_k) \tag{34}$$

For some point (x, y, z) in the fixed Cartesian system, the displacement time history of ground is,

$$U_{z,\mathrm{P}}(x, y, z, t) = \sum_{l=1}^{M} \tilde{U}_z(x - ct - a_l, y, z)\tilde{P}_l(\Omega_k)\mathrm{e}^{\mathrm{i}\Omega_k t} \tag{35}$$

Fourier transform Eq. (35) with respect to time t gives the spectrum of the vertical displacement $U_{z,\mathrm{P}}$,

$$S_{Uz}(x, y, \omega; \Omega_k) = -\left[\sum_{l=1}^{M} \tilde{P}_l(\Omega_k)\mathrm{e}^{-\mathrm{i}a_l(\Omega_k-\omega)/c}\right]^{\cdot} \left[\frac{1}{c}\mathrm{e}^{\mathrm{i}x(\Omega_k-\omega)/c}\int_{-\infty}^{+\infty}\tilde{U}_z(x_*, y)\mathrm{e}^{-\mathrm{i}x_*(\Omega_k-\omega)/c}\mathrm{d}x_*\right] \tag{36}$$

In reality, the wheel-rail unevenness is a random process extended along the track direction x, which may be decomposed into infinite contents with different wavelengths. The total response to the random wheel-rail unevenness is the superposition of the responses to each of the harmonic wheel-rail unevenness with a single wavelength. The power spectral density (PSD) response can therefore be derived as follows (Sheng *et al*. 2004),

$$P_{Uz}(x, y, z, \omega) = \sum_{k=1}^{+\infty}[\left|S_{Uz}(x, y, z, \omega; \Omega_k)\right|^2 + \left|S_{Uz}(x, y, z, \omega; -\Omega_k)\right|^2]^{\cdot} P_z(v_k)\Delta v + \left|S_{Uz}(x, y, z, \omega; 0)\right|^2 \tag{37}$$

in which $P_z(v_k)$ is the PSD of wheel-rail unevenness with the wave number v_k=1/λ_k and Δv the sampling interval; $S_{Uz}(x,y,z,\omega;0)$ represents the spectrum of vertical displacement response to the quasi-static axle loads (Takemiya and Goda, 1998) due to gravity of the train.

5 Numerical results and discussions

5.1 Verifications

Two typical examples in the literature of layered half-space will be computed based on the proposed Green's function. One is a layered half-space loaded by strip-distributed stress whose position is fixed on the surface, the other is still a layered half-space but excited by a moving strip load with a constant speed. Then the Green's function together with the train-track-ground model is further verified by an in situ test of the ground vibration caused by urban railway traffic.

5.1.1 Comparisons with existing numerical results

Responses of layered half-space to harmonic load with fixed position

The dimension of a layered half-space is shown in Fig. 3 (Rajapakse and Senjuntichai, 1996; Liu and Zhao,

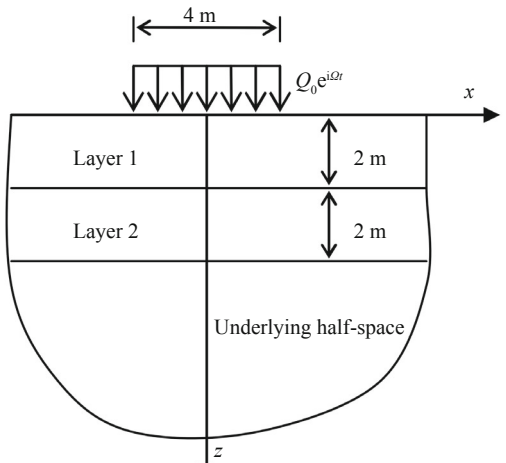

Fig. 3 Geometry of poroelastic layered systems C, D and dry elastic layered system, after Rajapakse and Senjuntichai (1996)

2013). Three sets of material properties, System C, System D and dry layers, are considered in this example. The values of poroelasitc parameters are listed in Table 1 and Table 2. Biot (1962) indicated that the mechanical behavior of a solid phase may approximate that of a single phase medium if the three parameters ρ_f, M and b approach 0. Accordingly, the properties of the dry layers are set as ρ_f= 0.0001kg/m^3, M = 0.0001 Pa and b =0; μ_0, λ_0, and ρ are assigned as Table 1; lost factor of the solid skeleton is η = 0.005.

The time-harmonic vertical load has a frequency Ω and an amplitude Q_0=1/4 Pa, acting on the surface of the layered half-space with a fixed position. The loading area is a strip perpendicular to the *x*-*z* plane. The problem considered here is therefore of plane strain (i.e., P-SV mode), which makes the *y*-direction's wave number γ=0. The load amplitude in the wave number domain is given by,

$$\bar{\tilde{\sigma}}_{zz} = \sin(2\beta)/(2\beta) \tag{38}$$

According to Eq. (27) the displacement of ground surface,

$$\bar{\tilde{U}}_z = \bar{\tilde{\delta}}_{44}(\beta, 0, \omega)\sin(2\beta)/(2\beta) \tag{39}$$

in which the frequency of ground vibration $\omega/2\pi$ is the same as the excitation frequency $\Omega/2\pi$ because the moving speed of the load is zero. Taking advantage of the FFT, the inverse Fourier transform of $\bar{\tilde{U}}_z$ from the β domain to the *x* domain can be carried out numerically. Altogether, 8192 points have been sampled with the interval of 0.001(rad·m^{-1}) in the FFT implementation.

Figure 4 shows the variation of the maximum displacements of ground surface as the frequency increases. The quantities shown are non-dimensionlized. The dimensionless displacement $U_z^* = \mu_0^{(1)}\tilde{U}_z / Q_0 h^{(1)}$ and the dimensionless frequency $\delta = \omega h^{(1)}\sqrt{\rho^{(1)}/\mu_0^{(1)}}$, where $\mu_0^{(1)}$, $h^{(1)}$, $\rho^{(1)}$ are the shear modulus, thickness and mass density of the material in the first layer. Also shown in Fig. 4 are the numerical results of Rajapakse and Senjuntichai (1996) and Liu and Zhao (2013). It can be seen that the results obtained by the proposed method are close to those of the references.

Responses of layered half-space to moving strip load

When the time-harmonic load moves along the *x* direction with a speed *c*, Eq. (39) becomes,

$$\bar{\tilde{U}}_z = \bar{\tilde{\delta}}_{44}(\beta, 0, \Omega - \beta c)\sin(2\beta)/(2\beta) \tag{40}$$

The inverse Fourier transform from the β domain to the space domain yields the vibration amplitude $\tilde{U}_z(x_*)$ in the moving frame of reference $x_* = x - ct$. For a particle of the ground surface, e.g., the point situated at the origin

Table 1 Material properties of the layered system excluding the values of *b*, after Rajapakse and Senjuntichai (1996)

	μ_0 (MPa)	λ_0 (MPa)	M (MPa)	ρ (kg·m^{-3})	ρ_f (kg·m^{-3})	m (kg·m^{-3})	α
First layer	250	500	2500	2000	1000	3000	0.95
Second layer	125	188	1880	1600	1000	1800	0.98
Underlying half-space	1000	1000	2000	2400	1000	4800	0.90

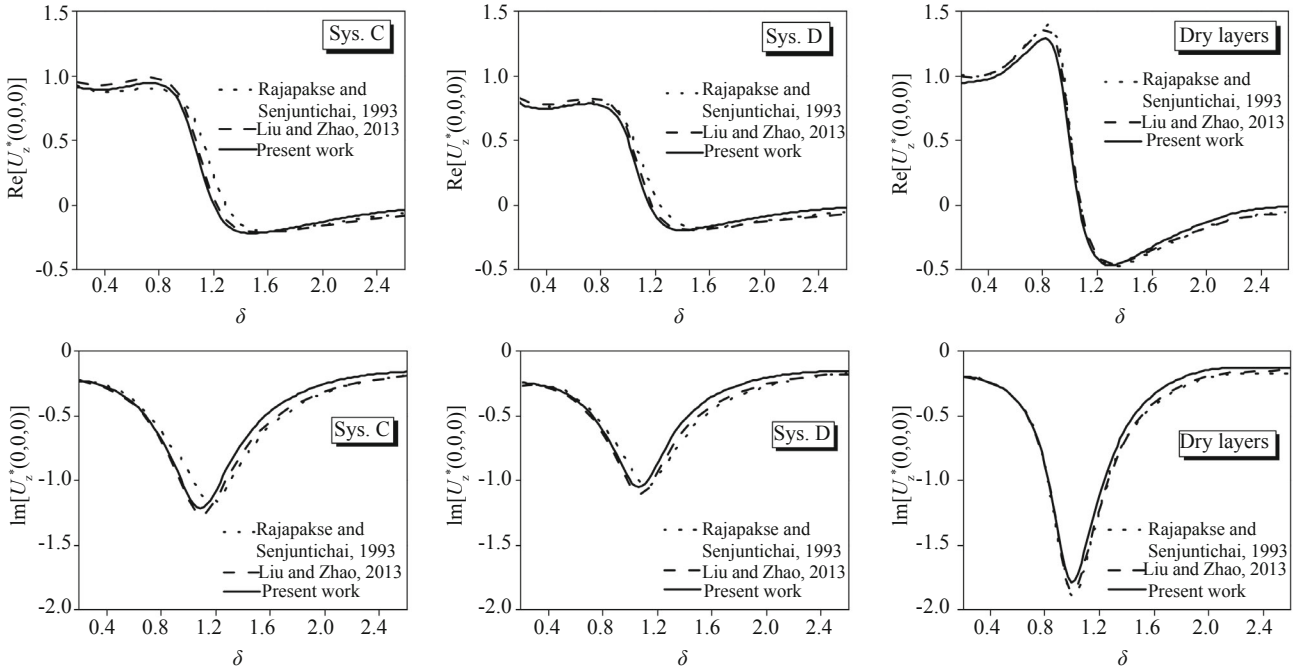

Fig. 4 Maximum vertical displacements of the ground surface due to time-harmonic strip loads with a fixed position

Table 2 Values of parameter *b* for different poroelastic layered systems, after Rajapakse and Senjuntichai (1996)

	First layer $b^{(1)}$ (MPa·s·m^{-2})	Second layer $b^{(2)}$ (MPa·s·m^{-2})	Half-space $b^{(3)}$ (MPa·s·m^{-2})
System C	0.30	0.75	4.50
System D	7.50	0.75	4.50

(0, 0) in Fig. 3, the time history of vibration may be computed as,

$$U_z(x,t)=\tilde{U}_z(x-ct)\mathrm{e}^{\mathrm{i}\Omega t} \tag{41}$$

For a point located inside the ground, other quantities involved have to be obtained before U_z is calculated. The displacements of ground surface $\boldsymbol{u}_0^1$ should be computed in terms of Eq. (25), where the stress vector $\boldsymbol{\sigma}_0^1=\{0,0,0,\sin(2\beta)/(2\beta)\}^{\mathrm{T}}$. Then the functions $\boldsymbol{A}^1$ and $\boldsymbol{B}^1$ are worked out by solving Eq. (19), and $\boldsymbol{A}^{j+1}$ and $\boldsymbol{B}^{j+1}$ may be determined in terms of Eq. (21) successively. The displacement $\tilde{U}_z$ at an arbitrary depth z is therefore obtained by Eq. (18).

The computed time histories of dimensionless U_z at (0, 0) point of ground D are presented in Fig. 5, where the time t = 0 corresponds to the moment that the center of the load exactly passes the origin with the speed c = 20m/s. In the case of quasi-static load (i.e., Ω = 0), as shown in Fig. 5a, the particle moves gradually down to a maximum and then come back to its original location. No upward displacement has been observed in the time history. In contrast, if the frequency of load Ω is NOT zero, the particle oscillates up and down repeatedly, as shown in Fig. 5(b).

One of the properties of a fluid-filled porous medium is the existence of P2 (or slow P) wave. It can be seen in Eq. (15) that the vertical displacement $\tilde{U}_z$ is composed of eight parts, of which two are related to the P2 wave via the parameter $\xi_{\mathrm{p}2}$. The summation of the two parts, $\xi_{\mathrm{p}2}g_2A_2\,\mathrm{e}^{-\xi_{\mathrm{p}2}z}-\xi_{\mathrm{p}2}g_2B_2\,\mathrm{e}^{\xi_{\mathrm{p}2}z}$, is called Slow P Wave Effect, and its time histories are also plotted in Fig. 5. It is interesting that the slow P wave effect is not in-phase with, sometimes even inverse, to the displacement of soil skeleton, though the effect is actually a part of the U_z according to Eq. (15). This result is consistent with the idea that in the fluid-borne slow P wave, the fluid phase moves in the opposite direction to the solid phase (Lo *et al*., 2007). This motion of fluid may lead to an inverse effect on the displacement of the solid phase, which may counteract the displacement of the skeleton-borne fast P wave and shear wave. The total value of solid displacement is a combined effect of slow P wave, fast P wave and shear wave. It should be mentioned that the slow P wave effect can be quite notable, as shown in this numerical example for silty sand under moving traffic load. This indicates that though the slow P wave attenuates rapidly and can hardly be observed in the field (Klimentos and Mccann, 1988), its effect should not be neglected in the case of moving excitations, because the slow P wave may be excited and carried by the moving loads.

Another typical stratified poroelastic ground model (Siddharthan *et al*., 1993b; Theodorakopoulos, 2003) is shown in Fig. 6, where the soil is supposed to be a layer of medium dense sand beneath which is impermeable bedrock. The material properties for the model are listed in Table 3. Because the example neglected the compressibility of porous fluid (Siddharthan *et al*. , 1993a, b), an extraordinary large value has been assigned to the parameter M which describes the relative compressibility among skeleton, solid grain and fluid. In order to simulate the impermeable and fixed boundary, large values are assigned to the Lamé constants, the mass density and the parameter M, while very small values are set to the permeability and porosity for the underlying half-space. The strip load on the ground has a constant magnitude Q_0= 400 kPa.

Figure 7 presents the peak value of U_z inside the

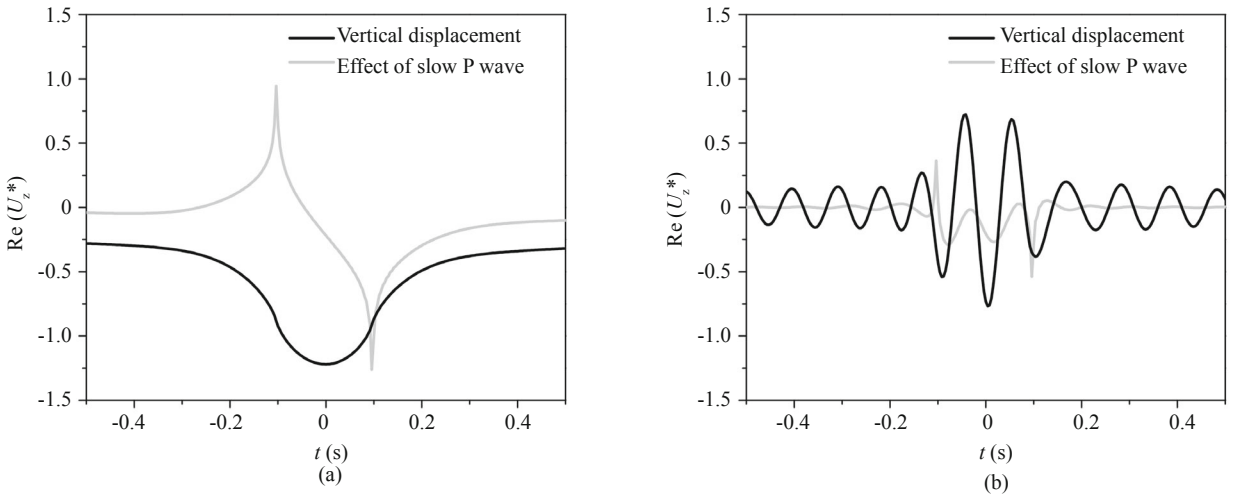

Fig. 5 Time domain responses at point (0,0) of poroelastic layered systems D subject to moving loads, with speed = 20 m/s. (a) Frequency of load $\Omega/2\pi$ = 0; (b) Frequency of load $\Omega/2\pi$ = 10 Hz

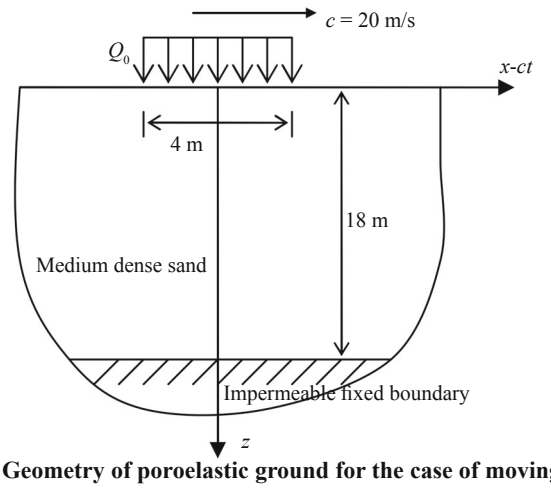

Fig. 6 Geometry of poroelastic ground for the case of moving strip load

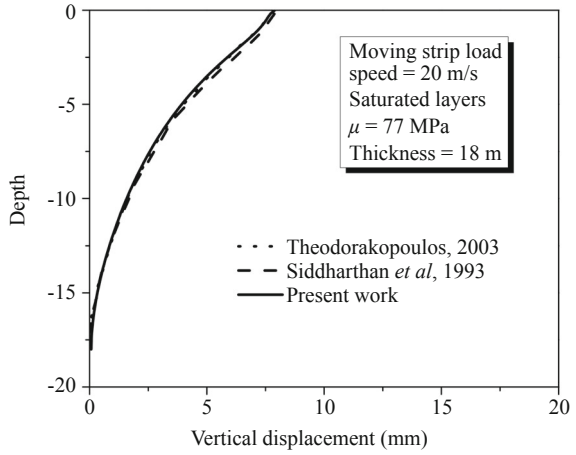

Fig. 7 Variation of maximum vertical displacement with depth of ground excited by moving strip load

Table 3 Material properties of the layered system for the case of moving strip load

	$h^{(j)}$ (m)	μ_0 (MPa)	λ_0 (MPa)	M (MPa)	ρ (kg·m^{-3})	ρ_f (kg·m^{-3})	k (m·s^{-1})	τ	α	η	φ
Sandy layer	18	77	180	1.5×10^8	1816	1000	1.0×10^{-5}	1.0	1.0	0.05	0.40
Underlying half-space	∞	20000	15000	1.5×10^9	4500	2000	1.0×10^{-7}	1.0	1.0	0.05	0.05

ground, where the results from the two above references are also depicted. The maximum displacement attenuates in the ground as the depth increases. Since the computed results have again been very close to those of the references, it may be concluded that the proposed Green' function works properly.

5.1.2 Comparison with data measured in the field

Ground vibrations were measured at a location (40.4118°N and 116.2096°E, identified by GPS) beside Line 13 of the Beijing Urban Railway (Wang *et al*., 2011), where the trains traveled between the stations of Huilongguan and Huoying with a speed about 60km/h (i.e., 17 m/s) along the track on the ground surface. The DKZ5 train, manufactured by Changchun Railway Vehicles Co., Ltd, consists of two locomotives and two carriages. Figure 8 shows the configuration of the train. Each of the vehicles is supported by two bogies and has four axles. The track in the measuring section is of the classic ballast type. The stochastic characteristics of the wheel-rail random unevenness were obtained by an inversion procedure (Wang *et al*, 2012). Figure 9 gives the PSD of the wheel-rail unevenness with respect to the spatial wavelength along the direction of the track.

A soil investigation was carried out in the measuring section. Figure 10 shows the plan of four boreholes BH1-BH4 near the track. The top soil is a layer of miscellaneous fill that is about 0.8 m thick. A silt layer under laid the top soil to a depth of 15 m below the ground surface. The underlying soils are fine sand and silty clay. Figure 11 gives the soil profile of the ground, where the shear wave velocities were measured by suspension logging instruments.

Accelerometers were installed at five points of the ground surface and arranged in a line perpendicular

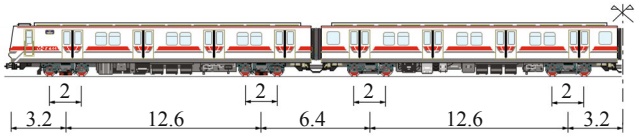

Fig. 8 Configuration of the urban train (dimensions in meter)

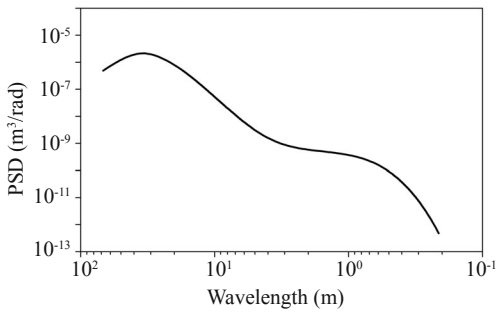

Fig. 9 Power spectral density for the wheel-rail unevenness of the Line 13, Beijing Urban Railway, after Wang *et al.*, 2012

to the track, as shown in Fig. 10. The distances of the observation points to the track centerline were 10 m, 20 m, 40 m, 50 m and 60 m, respectively. Acceleration time histories were measured with a sampling frequency of 200 Hz during the passage of an urban train. Altogether, 80 time histories were obtained for the passage of 16 trains.

Figure 12 shows one group of the vertical acceleration time histories. The PGAs (peak ground accelerations) are 0.23 m/s^2, 0.16 m/s^2, 0.04 m/s^2, 0.02 m/s^2 and 0.02 m/s^2, respectively, at the observation points of P1 to P5. This indicates that in the immediate vicinity of the track, the vibration attenuates very quickly from P1 to P3, whereas

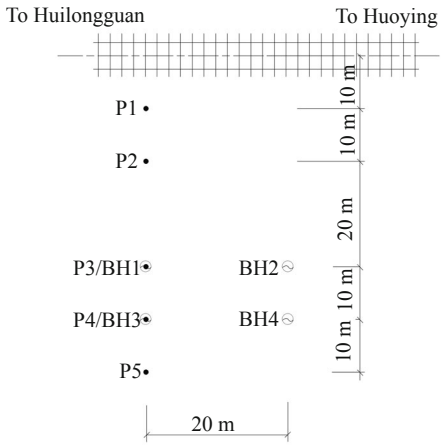

Fig. 10 Plan of the observation points on the ground surface

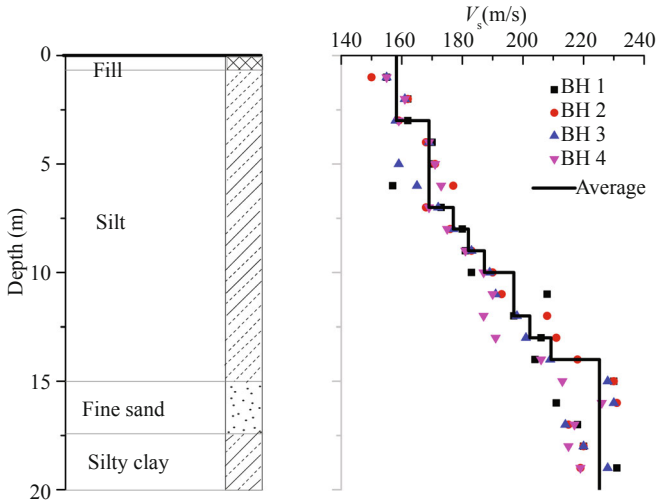

Fig. 11 Soil profile and shear wave velocity

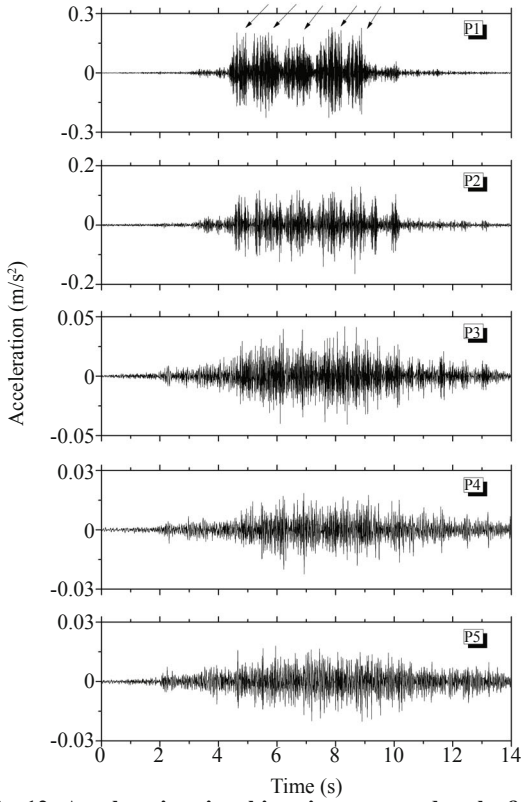

Fig. 12 Acceleration time histories measured at the five points of the ground surface during the passage of an urban train

in the further area from P3 to P5, the attenuation is slower.

The time history at the nearest observation point P1 has five apparent 'groups', as indicated by the five arrows in Fig. 12. These are the results of the passage of five groups of wheels. Each vehicle in the urban train has two bogies under the two ends of the car body. At one connection of two vehicles, there is a group of wheels under the bogies of the two neighboring ends. The train has four vehicles; consequently, there are three wheel-groups under the three connections. Together with the two wheel-groups under the first and last bogies of the train, the number of the groups totals five. The wheel-group effect can be easily identified in the time history of P1. However, when the distance increases to 20m or further, because of the complicated interference of vibrations, the effect can hardly be seen in the time histories.

By using the periodogram method, PSDs of acceleration were estimated based on the recorded time histories, as shown in Fig. 13. Within the area from 10 m to 60 m beside the track, the main frequency range of ground vibration is from 10 Hz to 80 Hz. Higher frequency contents dominate the vibrations of near points, and lower frequency vibrations are the main contents for the further points, which indicates that higher frequency contents attenuate more quickly than lower ones with the distance from the track increases.

The PSD of acceleration can be transformed to the vibration acceleration levels (VALs) at the center frequencies of one-third octave bands. In terms of the China National Standard, *measurement method of environmental vibration of urban area (GB10071-88)*,

$$\mathrm{VAL} = 20\lg(\ddot{U}_{z,\mathrm{rms}} / a_0) \tag{42}$$

in which a_0=1×10^{-6} m/s^2 is the reference acceleration; $\ddot{U}_{z,\mathrm{rms}} = \sqrt{\int_{\omega_l}^{\omega_u} P_{\ddot{U}z}\,\mathrm{d}\omega}$ is the effective value of the vertical acceleration; $P_{\ddot{U}z}$ is the PSD of the acceleration; and ω_l

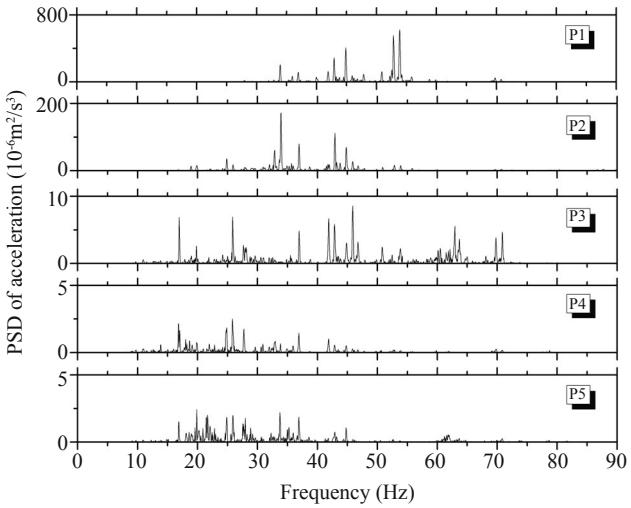

Fig. 13 PSDs of accelerations at the five points of the ground surface

and ω_u are the lower and upper limits of the one-third octave band. The estimated vibration levels based on the observed data are plotted in Fig.14.

The procedure of section 4 is used to simulate the field test. Parameters needed for modeling the train and the track are listed in Table 4 and Table 5, respectively, where the values are estimated based on design documents. Table 6 shows the ground soil properties from the soil investigation. The ground water table of this site is quite low, so very small values are assigned to the three parameters as M = 0.0001 Pa, b = 0 and ρ_f= 0.0001 kg/m^3. The computed PSDs of ground vibration are also transformed to the vibration levels, as shown in Fig. 14. It can be seen that in general, the agreements between the computed and the observed results are quite good at the observation points with different distances to the track. This indicates that the proposed Green's function, together with the train-track-ground model, is able to properly simulate the ground vibration caused by railway traffic.

5.2 More results of numerical simulation

As the ground water effect is difficult to investigate by the in situ observation, the proposed model is employed to numerically study the train-induced vibrations of

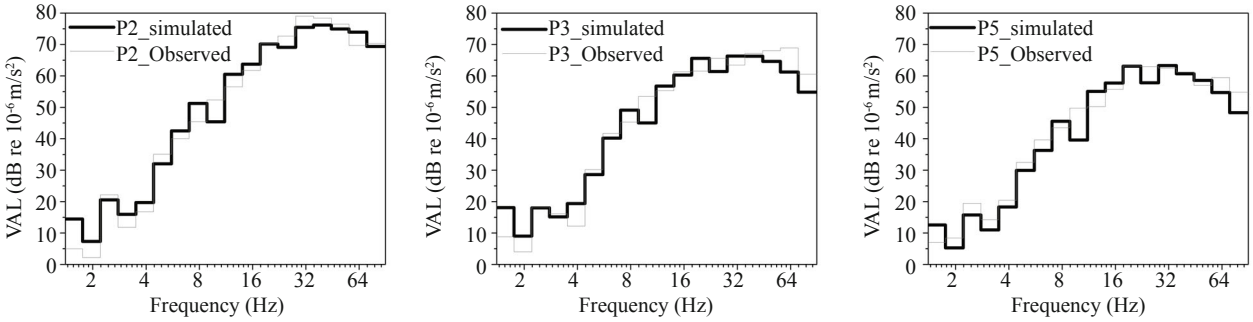

Fig. 14 Comparison between the simulated values and the observed values of the vibration acceleration levels (VALs) at the observation points on the ground surface

Table 4 Parameter values for the vehicles

Parameter	Unit	Carriage	Locomotive
Mass of the car body	kg	4.5×10^4	5.0×10^4
Mass of bogie	kg	2.8×10^3	3.0×10^3
Mass of wheelset	kg	1.8×10^3	1.8×10^3
Pitch inertia moment of the car body	kg·m^2	1.4×10^6	1.5×10^6
Pitch inertia moment of the bogie	kg·m^2	2.2×10^3	2.1×10^3
Primary vertical stiffness per axle	N/m	2.5×10^6	2.5×10^6
Secondary vertical stiffness per axle	N/m	1.0×10^6	1.0×10^6
Primary vertical viscous damping	N·s/m	1.2×10^5	8.0×10^4
Secondary vertical viscous damping	N·s/m	1.1×10^5	6.0×10^4
Distance between bogie centers	m	12.6	12.6
Distance between axles under a bogie	m	2.0	2.0
Radius of the wheel	m	0.42	0.42
Total length of the car	m	19.0	19.0

Table 5 Parameter values for the track structure

Component	Notation	Parameter	Value
Rail	m_R	Mass per unit length	121 kg/m
	E_0I	Flexural rigidity	1.3×10^7 N·m^2
	η_R	Hysteric damping ratio	0.005
Rail pad	k_{p0}	Undamped stiffness	3.5×10^8 N/m^2
	η_P	Hysteric damping ratio	0.075
Sleeper mass	m_s	Mass per unit length	416 kg/m
Layer of ballast embankment	m_B	Mass per unit length	2400 kg/m
	k_{B0}	Undamped stiffness per unit length	1.45×10^7 N/m^2
	η_B	Hysteric damping ratio	0.05
	2_{bl}	Contact width with the ground	4.50m

Table 6 Parameter values for the ground

$h^{(j)}$ (m)	μ_0 (MPa)	λ_0 (MPa)	ρ (kg/m^3)	V_s (m/s)
3.0	45	67	1800	158
4.0	56	84	1950	169
1.0	63	94	2000	177
1.0	65	97	1950	183
1.0	70	105	2000	187
2.0	74	111	1900	197
1.0	84	126	2050	202
1.0	85	128	1950	209
∞	99	148	1950	225

ground with shallow water table. For this purpose, an appropriate number of layers and the thickness of each layer for the poroelastic half-space should be determined. The geometric parameters depend on both soil profiles in the field and intentions of the modeling. Generally speaking, a model ground with many layers seems closer to the reality than the one with several layers. Too many layers, however, might contribute too much influence on the simulation. The results can therefore be too complicated to show useful meanings. The simulation presented in this section aims to reveal general features of water-saturated soil layers under railway, rather than for a specific engineering project. Thus the ground is represented by a simple model that consists of two layers and one underlying half-space, as listed in the Table 7. The thicknesses of the soil layers are determined by taking account of the depth of the ground, within which the energy of the Rayleigh wave cannot be ignored. As observed in the field, the main frequency content ranges are from 10Hz to 80Hz for the ground vibration from trains. For the phase velocity of about 200m/s, the corresponding range of Rayleigh wave length is approximately from several meters to over twenty meters. The 8m thick layers make it possible that all interfaces of soil within the depth of the Rayleigh wave have an impact on the ground vibration.

The material for underlying half-space is selected to be a water saturated Berea sandstone, which is a sedimentary rock whose grains are predominantly sand sized and composed of quartz bonded by silica (Mesgouez & Lefeuve-Mesgouez, 2009; Gerasik and Stastna, 2008). The material of the second layer is a water saturated sand of Mol (Mesgouez and Lefeuve-Mesgouez, 2009; Degrande *et al*., 1998), which is also composed of quartz particles but is much softer than the underlying Berea sandstone. The surface layer has the same properties as those of the second layer, except for the parameters of ρ_f, M and b whose values are very small to represent a dry layer of ground surface.

5.2.1 Vibration levels of ground surface

The simulated vibration levels at three surface points, with distances of y = 10 m, 20 m and 30 m from the track, respectively, are compared in Fig. 15. Overall, the surface vibration tends to decrease was the distance from the track increases. From the point of y = 10 m to the point of y = 20 m, vibration levels of all frequencies are decreasing. The attenuation values in the frequency bands of 10 Hz and 12.5 Hz are smaller than those in other frequency bands. From y = 20 m to y = 30 m, the attenuation is slower than that from 10 m to 20 m, especially in the very low frequency bands under 4 Hz.

5.2.2 Patterns of vibration under midline of track

As mentioned in Section 4, the random wheel-rail unevenness can be deemed as a superposition of a series of harmonic unevenness, and the random vibration of ground is a combined effect of the vibrations caused by all harmonic contents of the unevenness. Assuming that the amplitude of harmonic unevenness is 1mm, and the frequencies perceived by wheels $\Omega_k/2\pi$ = 0, 4, 8, 16, 31.5, 63 Hz, respectively, calculate the ground vibration in the moving coordinate system (x_*= x-ct, y, z) in terms of Eq. (34). Note that under the condition of $\Omega_k/2\pi$ = 0, no fluctuation occurs at wheel-rail contact points, and each of the wheel-rail load is the quasi-static load whose magnitude equals the gravity of train shared by the wheel. The computed patterns of displacement Re($\tilde{U}_{z,\mathrm{P}}$) and excess pore pressure Re($\tilde{P}_{\mathrm{f,P}}$) at y = 0, z = 1.2 m (the location is directly below the midline of the track

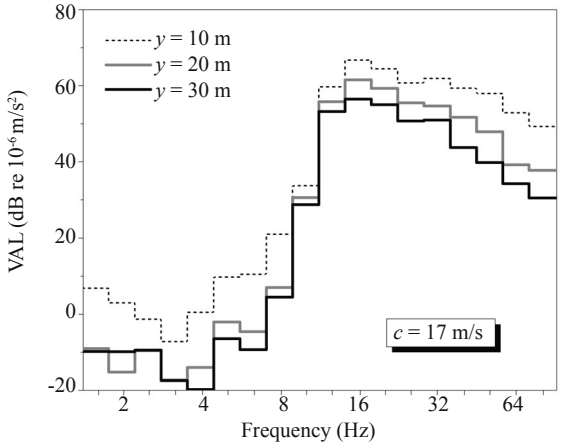

Fig. 15 Calculated VALs at three surface points of the poroelastic ground, with different horizontal distances to the midline of the track

Table 7 Material properties of the poroelastic layered ground for the case of coupled train-track-ground vibration

	$h^{(j)}$ (m)	μ_0 (MPa)	λ_0 (MPa)	M (MPa)	ρ (kg·m^{-3})	ρ_f (kg·m^{-3})	k (m·s^{-1})	τ	α	η	φ
First layer	1.0	112	223	0.0001	2010	0.0001	1.000×10^{8}	1.789	1.0	0.05	0.388
Second layer	7.0	112	223	5178	2010	1000	1.019×10^{-4}	1.789	1.0	0.05	0.388
Underlying half-space	∞	7020	5690	9710	2315	1000	3.600×10^{-6}	2.400	1.0	0.05	0.200

and within the saturated sand near the top of the second layer) are presented in Fig. 16. In each of the graphs, the left tick labels are for displacement and the right for pore pressure. Downward displacement and compressive pressure are supposed to be positive in this figure. The train is moving toward the positive direction of the *x-ct* axis, and is at the position from *x-ct* = 0 to *x-ct* = -76 m.

The curves of $\Omega_k/2\pi = 0$ show that the displacement shape under the quasi-static loads is quite similar to the ground settlement under static loads. The displacement of any point is positive, which indicates that the soil skeleton has only downward displacement without upward fluctuation. The peaks of the displacement curve correspond right to the locations of bogies. The excess pore pressure, however, is obviously different from its distribution under static loads. Both positive and negative values of the pressure appear, which means that the pore water pressure increases somewhere but decreases elsewhere in the ground. Each positive peak is under the front wheel of a bogie and does not appear under the back wheel of the bogie, which may be interpreted as an effect of moving load. When the front wheel is coming, the soil is squeezed, and the water pressure is rising. After the front wheel rolls away, the resilient dilation of the compressed soil may result in a sharp drop of the water pressure. The pressure cannot reach a positive peak when the back wheel of the bogie arrives, though it may compensate for the water pressure to some extent.

Once the wheel-rail force frequency $\Omega_k/2\pi$ is not 0, the displacements and stresses of the ground are time-harmonically varying in the moving reference system.

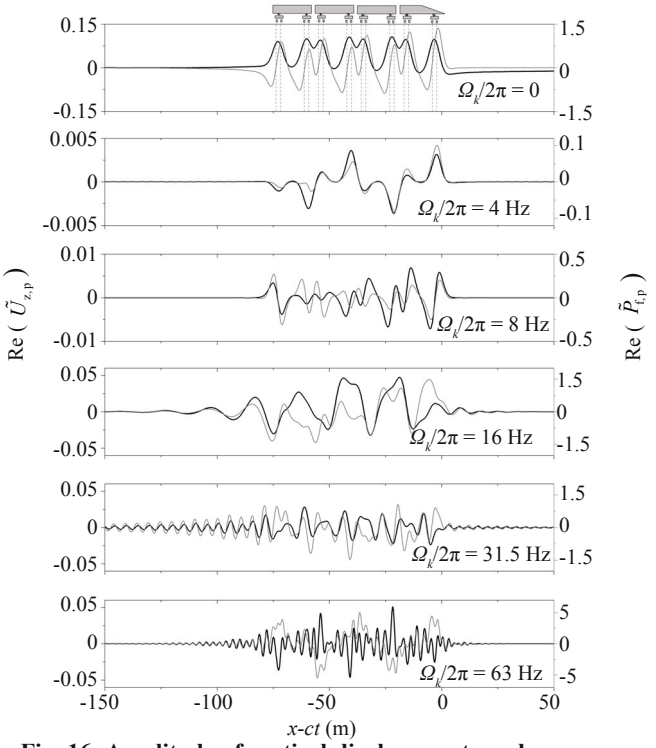

Fig. 16 Amplitude of vertical displacements and excess pore pressures in the moving coordinate system (*x-ct*, *y*, *z*) at *y* = 0, *z* = 1.2 m

The curves shown are the amplitudes of the vibration. In the condition of very low frequency ($\Omega_k/2\pi$ = 4 Hz), the curves of displacement and the excess pore pressure are similar, especially under the four bogies of the first two vehicles. When the excitation frequency becomes higher, the two curves are no longer in phase. The vibrations attenuate very quickly ahead of and behind of the train when the frequency $\Omega_k/2\pi$ is not more than 8Hz. For higher frequencies of wheel-rail excitation, the vibration has a much wider influence range along the track direction.

5.2.3 Vibration attenuation with depth under midline of track

The maximum of the absolute value of the function $\tilde{U}_{z,\mathrm{P}}$ along the *x-ct* axis represents the vibration intensity of the vertical displacement. Fig. 17 shows the variation of this intensity under the midline of the track when the depth increases in the ground. Also shown are the intensities of excess pore water pressure max[abs($\tilde{P}_{\mathrm{f,P}}$)], and the vertical total stress max[abs($\tilde{\sigma}_{zz,\mathrm{P}}$)]. The frequency of wheel-rail force is selected to be 4, 16 and 64Hz, respectively, to represent low, medium and high frequency of excitation.

In the first layer, the computed excess pore pressure are almost zero, which indicates that the propose method is able to make a proper simulation for a dry soil layer. The vertical total stress has its maximum on the ground surface in the case of the low frequency excitation. In the case of medium or high frequency, the maximum appears in the first layer but under the surface of the ground. The vertical displacement decreases as the depth increases within the first layer. It should be noted that the three displacement curves have different scales in Fig. 17, and the attenuation is much faster in the high frequency case than that in the low frequency case.

The second layer is from *z* = 1 m to *z* = 8 m. As the depth increases, the excess pore pressure increases to its first peak very quickly, then reduces to a valley value near the midpoint of the layer. When approaching the underlying half-space, the excess pore pressure increases to its second peak. This result properly reflects the fact that the permeability of Berea sandstone is far lower than that of Mol sand, which results in a local condition of poor drainage at the bottom of the sandy layer of Mol, and therefore increases the excess pore pressure to the second local peak. The vertical displacements and total stresses, in general, keep attenuating in the second layer. At the bottom of the second layer, the displacements almost decrease to zero while the total stresses still have substantial magnitudes to be delivered into the underlying half-space. These results indicate that the hard underlying Berea sandstone has effectively constrained the bottom of the second layer.

In the underlying half-space, the excess pore pressure reduces sharply to a very small value while the vertical total stress attenuates much slower, which indicates substantial portion of stress is transferred to the very stiff skeleton of the Berea sandstone.

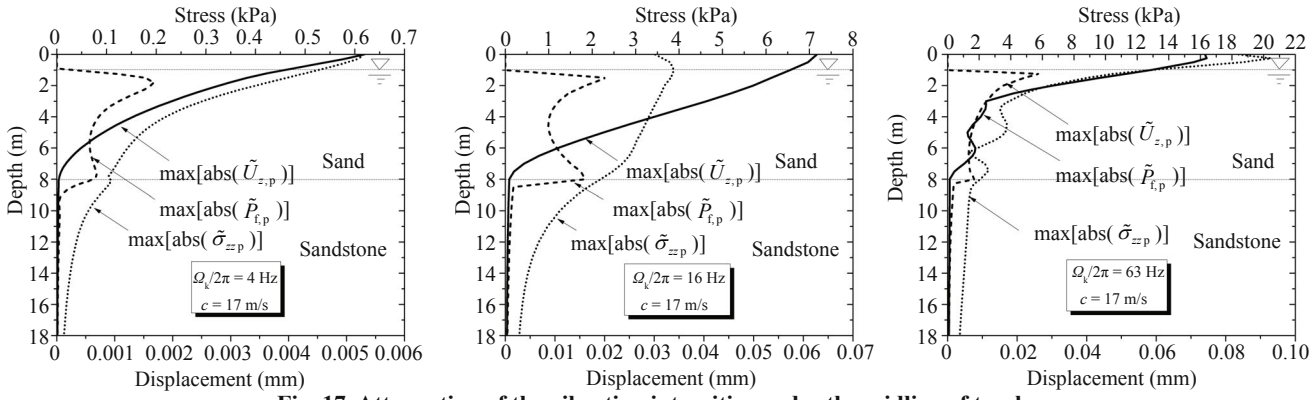

Fig. 17 Attenuation of the vibration intensities under the midline of track

5.2.4 Two-dimensional patterns of vibration in the ground

The results presented in Fig. 16 and Fig. 17 are some of the responses within the vertical plane of $y = 0$. Fig. 18a shows a two dimensional pattern of the displacement Re($\tilde{U}_{z,P}$) in the horizontal plane of z = 1.2 m. In this case, the frequency of the wheel-rail force is 4 Hz, which is caused by the wheel-rail unevenness with the wave length of λ_k = 4.25 m at the train speed of 60 km/h (or 17m/s). The vertical displacement is largely limited within the area under the train, and attenuates very quickly along the two sides of the track.

If the speed of the train is set to be 220 m/s, which is the value of the Rayleigh wave velocity of the medium in the first layer, the frequency of wheel-rail force becomes $\Omega_k = c/\lambda_k$ = 220/4.25 = 52 Hz. Fig. 18(b) gives the recomputed displacement Re($\tilde{U}_{z,P}$) at z = 1.2 m. Both the amplitude and the influence area are much larger than those in the Fig 18(a). Because the train is traveling almost together with the surface wave, no ground vibration is found propagating ahead of the train in the Fig. 18(b). Intensive vibrations propagate toward the side-back of the train, which results in a series of Mach Cone. According to many reports (e.g., Sheng *et al.*, 2003; Adolfsson *et al.*, 1999; Takemiya, 2003; Madshus and Kaynia, 2000), Sweden's X2000 High Speed Train was subjected to severe vibration when traveling near Ledsgard at a speed approaching the Rayleigh wave velocity of the soft soil ground. The computed result indicates that the proposed approach is able to model this extreme effect. In addition, Figure 19 shows the computed vibration levels in the condition of random wheel-rail unevenness. Compared with the results of the train speed c = 17m/s, vibration levels in every frequency band are remarkably enhanced when the train speed approaches the Rayleigh wave velocity.

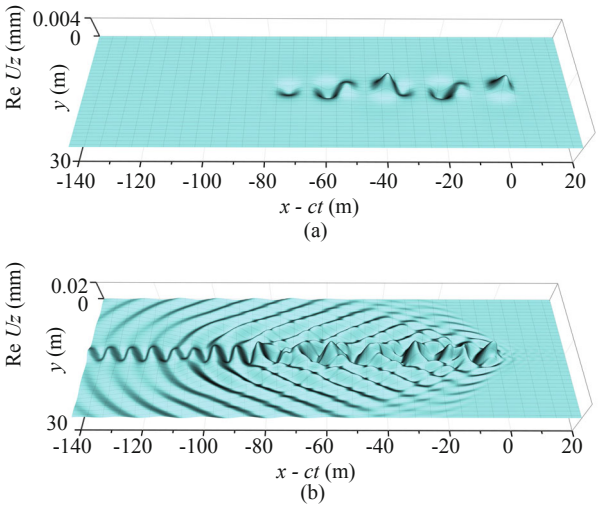

Fig. 18 Vertical displacement of ground surface when a train running on a track with different speeds, (a) c = 17 m/s; (b) c = 220 m/s

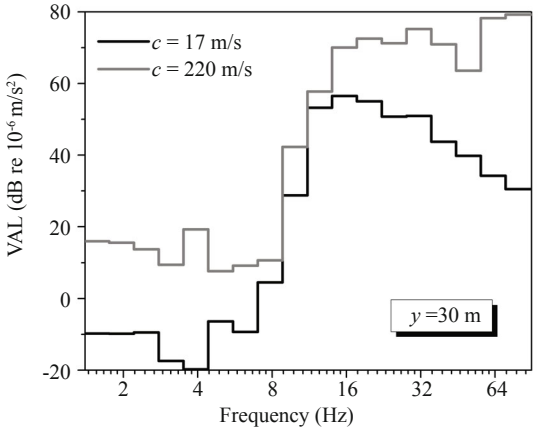

Fig. 19 Comparison of vibration levels due to different speeds of train

6 Conclusion

Dynamic Green's function is a mathematical representation of ground, which plays a key role in the coupled vibration model of train-track-ground. The proposed Green's function allows for the effects of the solid-fluid dynamic interaction, stratified configuration of deposits and three-dimensional propagation of waves in the ground. Numerical results agree with those in the literature and are close to an in situ test of train-induced ground vibration.

The computed responses to the random wheel-rail unevenness are able to simulate the distribution features

of the ground surface vibration, i.e., the vibration attenuates faster in the immediate vicinity of the track than in the area far from the track. Typical features of ground settlement and pore pressure distribution under quasi-static loads can be evaluated by the proposed approach. In the case of harmonic wheel-rail unevenness, the computed displacement caused by high frequency wheel-rail force may attenuate more quickly in the ground, compared to low and medium frequency excitation. The variations of the displacement, total stress and pore pressure in the ground reflect the variations of the soil properties of the ground layers. When the speed of the train is set to be the velocity of the Rayleigh wave, the Mach Cone, as expected, is represented in the computed vibration pattern.

Although the Green's function has been proposed to study ground vibration from the train, it may also be useful in modeling other geotechnical problems of moving excitations such as vibrations of pavement from highway traffic, and dynamic responses of seabed to ocean wave. It should be mentioned that the procedure described herein cannot deal with the problem of buried excitations, which has been well investigated by other researchers as previously mentioned.

The Fortran programs of the Green's function together with the train-track-ground coupled vibration have been developed by the first author. Researchers interested in the programs are welcome to contact Wang-futong@126.com to receive a copy of the codes.

Acknowledgement

This research is supported by the National Natural Science Foundation of China (Key Project, Grant No. 50538030), Postdoctoral Science Foundation of China (Grant No. 2013M531084) and Natural Science Foundation of Heilongjiang Province of China (Grant No. E201221).

References

Adolfsson K, Andreasson B, Bengtsson P and Zachrisson P (1999), "High Speed Train X2000 on Soft Organic Clay-measurements in Sweden," *Proceedings of the Twelfth European Conference on Soil Mechanics and Geotechnical Engineering, 3*, Amsterdam, Netherlands, 1713–1718.

Apsel RJ and Luco JE (1983), "On the Green's Functions for a Layered Half-space," Part II. *Bulletin of the Seismological Society of America,* **73**(4): 931–951.

Beskou ND and Theodorakopoulos DD (2011), "Dynamic Effects of Moving Loads on Road Pavements: A Review," *Soil Dynamics and Earthquake Engineering,* **31**(4): 547–567.

Biot MA (1962), "Mechanics of Deformation and Acoustic Propagation in Porous Media." *Journal of Applied Physics,* **18**(4): 1482–1498.

Cai Y, Cao Z, Sun H and Xu C (2009), "Dynamic Response of Pavements on Poroelastic Half-space Soil Medium to a Moving Traffic Load," *Computers and Geotechnics,* **36**(1-2): 52–60.

Cao Z, G Cai and Y Q, Sun HL and Xu CJ (2011), "Dynamic Responses of a Poroelastic Half-space from Moving Trains Caused by Vertical Track Irregularities," *International Journal for Numerical and Analytical Methods in Geomechanics,* **35**(7): 761–786.

Degrande G, De Roeck G, Van den Broeck P and Smeulders D (1998), "Wave Propagation in Layered Dry, Saturated and Unsaturated Poroelastic Media," *International Journal of Solids and Structures,* **35**(34): 4753–4778.

Gerasik V and Stastna M (2008), "Poroelastic Acoustic Wave Trains Excited by Harmonic Line Tractions," *Proceedings of the Royal Society*, *A Mathematical Physical & Engineering Sciences,* **464**(2090): 491–511.

Haskell NA (1953), "The Dispersion of Surface Waves on Multilayered Media," *Bulletin of the Seismological Society of America,* **43**(1): 17–34.

Jin B, Yue ZQ and Tham LG (2004), "Stresses and Excess Pore Pressure Induced in Saturated Poroelastic Halfspace by Moving Line Load," *Soil Dynamics and Earthquake Engineering*, **24**(1): 25–33.

Klimentos T and Mccann C (1988), "Why is the Biot Slow Compressional Wave Not Observed in Real Rocks?" *Geophysics*, **53**(12): 1605–1609.

Lefeuve-Mesgouez G and Mesgouez A (2008), "Ground Vibration due to a High-speed Moving Harmonic Rectangular Load on a Poroviscoelastic Half-space," *International Journal of Solids and Structures*, **45**(11–12): 3353–3374.

Lefeuve-Mesgouez G and Mesgouez A (2012), "Three-dimensional Dynamic Response of a Porous Multilayered Ground under Moving Loads of Various Distributions," *Advances in Engineering Software*, **46**(1): 75–84.

Liu T and Zhao C (2013), "Dynamic Analyses of Multilayered Poroelastic Media Using the Generalized Transfer Matrix Method," *Soil Dynamics and Earthquake Engineering*, **48**: 15–24.

Lo W, Yeh C and Tsai C (2007), "Effect of Soil Texture on the Propagation and Attenuation of Acoustic Wave at Unsaturated Conditions," *Journal of Hydrology*, **338**(3–4): 273–284.

Lombaert G and Degrande G (2009), "Ground-borne Vibration due to Static and Dynamic Axle Loads of Intercity and High-speed Trains," *Journal of Sound and Vibration*, **319**(3–5): 1036–1066.

Lombaert G, Degrande G, Kogut J and François S (2006), "The Experimental Validation of a Numerical Model for the Prediction of Railway Induced Vibrations," *Journal of Sound and Vibration*, **297**(3–5): 512–535.

Lowe MJ (1995), "Matrix Techniques for Modeling

Ultrasonic Waves in Multilayered Media," *Ultrasonics, Ferroelectrics, and Frequency Control, IEEE Transactions on*, **42**(4): 525–542.

Lu J and Jeng D (2007), "A Half-space Saturated Poro-elastic Medium Subjected to a Moving Point Load," *International Journal of Solids and Structures*, **44**(2): 573–586.

Lu J, Xu B and Wang J(2009), "A Numerical Model for the Isolation of Moving-load Induced Vibrations by Pile Rows Embedded in Layered Porous Media," *International Journal of Solids and Structures*, **46**(21): 3771–3781.

Luco JE and Apsel RJ (1983), "On the Green's Functions for a Layered Half-space. Part I. *Bulletin of the Seismological Society of America*, **73**(4): 909–929.

Madshus C and Kaynia AM (2000), "High-speed Railway Lines on Soft Ground: Dynamic Behaviour at Critical Train Speed," *Journal of Sound and Vibration,* **231**(3): 689–701.

Mesgouez A and Lefeuve-Mesgouez G (2009), "Transient Solution for Multilayered Poroviscoelastic Media Obtained by an Exact Stiffness Matrix Formulation," *International Journal for Numerical and Analytical Methods in Geomechanics*, **33**(18): 1911–1931.

Rajapakse R and Senjuntichai T (1996), "Dynamic Response of a Multi-layered Poroelastic Medium," *Earthquake Engineering and Structural Dynamics*, **25**(10): 1165.

Rokhlin SI and Wang L (2002), "Stable Recursive Algorithm for Elastic Wave Propagation in Layered Anisotropic Media: Stiffness Matrix Method," *Journal of the Acoustical Society of America*, **112**(3 Pt 1): 822–834.

Sheng X, Jones CJC and Petyt M (1999a). "Ground Vibration Generated by a Harmonic Load Acting on a Railway Track," *Journal of Sound and Vibration*, **225**(1):3–28.

Sheng, X., Jones, CJC and Petyt, M. (1999b). Ground Vibration Generated by a Load Moving along a Railway Track. *Journal of Sound and Vibration, 228*(1), 129–156.

Sheng X, Jones CJC and Thompson, DJ (2003), "A Comparison of a Theoretical Model for Quasi-statically and Dynamically Induced Environmental Vibration from Trains with Measurements," *Journal of Sound and Vibration*, **267**(3): 621–635.

Sheng X, Jones CJC and Thompson DJ (2004), "A Theoretical Model for Ground Vibration from Trains Generated by Vertical Track Irregularities," *Journal of Sound and Vibration,* **272**(3–5): 937–965.

Siddharthan R, Zafir Z and Norris GM (1993a), "Moving Load Response of Layered Soil, I: Formulation," *Journal of Engineering Mechanics,* **119**(10): 2052–2071.

Siddharthan R, Zafir Z and Norris GM (1993b), "Moving Load Response of Layered Soil, II: Verification and Application," *Journal of Engineering Mechanics,* **119**(10): 2072–2089.

Sun H, Cai Y and Xu C (2010), "Three-dimensional Simulation of Track on Poroelastic Half-space Vibrations due to a Moving Point Load," *Soil Dynamics and Earthquake Engineering,* **30**(10): 958–967.

Takemiya H (2003), "Simulation of Track–ground Vibrations due to a High-speed Train: The Case of X-2000 at Ledsgard," *Journal of Sound & Vibration,* **261**(3): 503–526.

Takemiya H and Goda K (1998), "Wave Propagation/ Impediment in a Soil Stratum over Rigid Base due to Impulse/Moving Loads," *Proceedings of JSCE,* **605**(605): 161–169.

Theodorakopoulos DD (2003), "Dynamic Analysis of a Poroelastic Half-plane Soil Medium under Moving Loads," *Soil Dynamics and Earthquake Engineering,* **23**(7): 521–533.

Thomson WT (1950), "Transmission of Elastic Waves through a Stratified Solid Medium," *Journal of Applied Physics,* **21**(2): 89–93.

Wang FT, Tao XX, Cui GH, Xin Z and Liang DY (2011), "Test in Situ for Free Ground Vibration near Urban Railway Line," *Journal of Vibration & Shock,* **30**(5): 131–135.

Wang FT, Tao XX, Xie LL, Zheng X and Cui GH (2015), "Dynamic Green's Function of Stratified Ground with Saturated Soil Layers for Modeling Ground Vibration near Railway Track," *Chinese Journal of Geophyslcs-Chinese Edition*, **58**(8): 2948–2961.

Wang FT, Tao XX and Zheng X (2012). "Inversion of Excitation Source in Ground Vibration from Urban Railway Traffic," *Science China Technological Sciences,* **55**(4): 950–959.

Xu B, Lu J and Wang J (2007), "Dynamic Response of an Infinite Beam Overlying a Layered Poroelastic Half-space to Moving Loads," *Journal of Sound and Vibration*, **306**(1-2): 91–110.

Xu B, Lu J and Wang J (2008), "Dynamic Response of a Layered Water-saturated Half Space to a Moving Load," *Computers and Geotechnics*, **35**(1): 1–10.

Zheng P, Ding B, Zhao S and Ding D (2013), "3D Dynamic Green's Functions in a Multilayered Poroelastic Half-Space," *Applied Mathematical Modelling*, **37**(24): 10203–10219.

Appendix

$$\begin{cases} b_0 = \mathrm{i}b/\omega - m \\ b_1 = \dfrac{\lambda_c + \mu}{\mu} + \dfrac{\rho_f M \alpha}{b_0 \mu} \\ b_2 = \dfrac{M}{\mu}(\alpha + \dfrac{\rho_f}{b_0}) \\ d_i = \dfrac{(\lambda_c + 2\mu) - \rho V_{pi}^2}{\rho_f V_{pi}^2 - \alpha M} \qquad i = 1, 2 \\ g_i = b_1 + b_2 d_i \\ t_i = \rho_f g_i - M(\alpha + d_i)(\xi_{pi}^2 - \xi^2)/\omega^2 \\ t_{bi} = (g_i \alpha + t_i / b_0) M \omega^2 / V_{pi}^2 \\ t_{ci} = \alpha t_{bi} + \lambda(\xi_{pi}^2 - \xi^2) - 2\mu g_i \xi_{pi}^2 \end{cases} \tag{A1}$$

$$\boldsymbol{C}_{u+} = \begin{bmatrix} -\dfrac{t_1 \xi_{p1}}{b_0} & -\dfrac{t_2 \xi_{p2}}{b_0} & 0 & -\dfrac{\mathrm{i}\gamma}{\xi b_0}\rho_f \\ 0 & 0 & 1 & 0 \\ -\mathrm{i}\gamma g_1 & -\mathrm{i}\gamma g_2 & 0 & 1 \\ -\xi_{p1} g_1 & -\xi_{p2} g_2 & 0 & -\dfrac{\mathrm{i}\gamma}{\xi} \end{bmatrix} \tag{A2}$$

$$\boldsymbol{C}_{u-} = \begin{bmatrix} \dfrac{t_1 \xi_{p1}}{b_0} & \dfrac{t_2 \xi_{p2}}{b_0} & 0 & \dfrac{\mathrm{i}\gamma}{\xi b_0}\rho_f \\ 0 & 0 & 1 & 0 \\ -\mathrm{i}\gamma g_1 & -\mathrm{i}\gamma g_2 & 0 & 1 \\ \xi_{p1} g_1 & \xi_{p2} g_2 & 0 & \dfrac{\mathrm{i}\gamma}{\xi} \end{bmatrix} \tag{A3}$$

$$\boldsymbol{C}_{\sigma+} = \begin{bmatrix} -t_{b1} & -t_{b2} & 0 & 0 \\ 0 & 0 & \mu\xi & 0 \\ -2\mathrm{i}\mu\gamma g_1 \xi_{p1} & -2\mathrm{i}\mu\gamma g_2 \xi_{p2} & 0 & \mu(\xi + \dfrac{\gamma^2}{\xi}) \\ t_{c1} & t_{c2} & 0 & -2\mathrm{i}\mu\gamma \end{bmatrix} \tag{A4}$$

$$\boldsymbol{C}_{\sigma-} = \begin{bmatrix} -t_{b1} & -t_{b2} & 0 & 0 \\ 0 & 0 & -\mu\xi & 0 \\ 2\mathrm{i}\mu\gamma g_1 \xi_{p1} & 2\mathrm{i}\mu\gamma g_2 \xi_{p2} & 0 & -\mu(\xi + \dfrac{\gamma^2}{\xi}) \\ t_{c1} & t_{c2} & 0 & -2\mathrm{i}\mu\gamma \end{bmatrix} \tag{A5}$$